Palaeostress state around a rising salt diapir inferred from seismic reflection data

Qiang Zhang [*], Tiago Alves

3D Seismic Lab, School of Earth and Environmental Sciences, Cardiff University, Main Building, Park Place, Cardiff, CF10 3AT, United Kingdom

A B S T R A C T

A 3D seismic volume and borehole data from the Dutch North Sea are used to investigate the palaeostress state around a rising salt diapir. The results show radial, polygonal and keystone faults around the diapir of interest, which are separated into eight zones based on their geometry, strike and overall distribution. Principal fault families include: a) 400–3500 m long radial faults developed in flanking and corner areas of the salt diapir, and known to have accommodated the stretching resulting from its rise, b) 200–1500 m long polygonal faults providing a record of the stress conditions farther from radial faults, and c) 1000–1800 m long keystone faults controlled by the rise of a buried salt pillow during Paleogene tectonic inversion. Stress inversions for 10,401 interpreted faults reveal that the maximum principal palaeostress (σ_1) is close to vertical, whereas intermediate and minimum principal palaeostresses (σ_2 and σ_3) are sub-horizontal, though variable in their magnitudes and orientations. Palaeostresses in flanking zones of the salt diapir show marked differences when compared with corner zones, but the combination of minimum principal palaeostresses from all flanking and corner zones formed a triangular stress ring around the salt diapir. Importantly, the width of this stress ring was not only associated with the rise of the salt diapir, but also largely influenced by adjacent salt structures. Additionally, minimum principal palaeostresses estimated from polygonal fault systems are nearly normal to the boundary between polygonal and radial faults, implying that the rise of the salt diapir influenced the stress field in the outer part of its flanks. Stress inversion is shown here as a key method to understand the palaeostress state around the salt diapirs with triangular geometry and multiple growth stages, providing insights into their evolving stress states. This work also has implications to the analysis of salt diapirs, and their adjacent strata, in areas posed for carbon sequestration, gas storage, and the production of oil and gas.

1. Introduction

Salt diapirs are common structures of sedimentary basins in which evaporites are thick, mobile, and pierce their overburden strata (Jackson and Talbot, 1986; Jackson and Hudec, 2017). The strata above and flanking salt diapirs are usually deformed, forming arched roofs crossed by multiple salt-related fault families (Alsop, 1996; Davison et al., 1996, 2000a; Rowan et al., 1999). The formation and growth of these salt-related faults are controlled by the stress conditions associated with the salt diapirism per se (Vendeville and Jackson, 1992; Carruthers et al., 2013; Wenau and Alves, 2020; Zhang et al., 2022). For instance, radial faults extend outwards from salt diapirs to accommodate the circumferential stretching of their arched roofs (Jackson et al., 1994; Mandl, 1999; Stewart, 2006; Yin and Groshong, 2007), whereas keystone faults develop in the hinge zone of salt diapirs and form symmetric extensional grabens above them (Harding and Lowell, 1979; Rowan et al., 1999; Alves, 2012).

Salt-related faults may become favourable fluid flow paths, or seals, for fluid accumulated in subsurface reservoirs (Davison et al., 2000b; Cox et al., 2001; Gartrell et al., 2004). However, boreholes drilled near these reservoirs often record technical problems, leading to unforeseen costs or even their complete abandonment (Bradley, 1978; Langer and Heusermann, 2001; Dusseault et al., 2004). Most issues occur because rising salt diapirs impose significant stress perturbations on adjacent strata (Seymour et al. 1993; Dusseault et al., 2004; Sanz and Dasari, 2010; Van-der-Zee et al., 2011; Nikolinakou et al., 2014). In recent years, numerical and geomechanical models have been increasingly used to figure out the stress conditions around salt diapirs, the main drivers of this work being conventional oil and gas exploration (Luo et al., 2012; Nikolinakou et al., 2012, 2014; Teófilo et al., 2018;

Hooghvorst et al., 2020), the need to find new options regarding CO_2 and H_2 storage (Chiaramonte et al., 2008; Chang et al., 2011; Ouellet et al., 2011; Ozarslan, 2012; Maia da Costa et al., 2019), and analyses of seal competence above and within salt structures regarded as potential and feasible storage sites for compressed air (Warren, 2017; Gasanzade et al., 2021). Also known from the literature are structural analyses of mining prospects within, or near, halokinetic structures (Davison et al., 1996; Behlau and Mingerzahn, 2001; Van Gent et al., 2011). As key examples of recent work, Hooghvorst et al. (2020) used 3D static geomechanical models to predict stresses around salt diapirs in the Tarfaya Salt Basin, Morocco. In addition, Lagrangian finite element forward models were used to discern the effect of deposition and salt movement in local stresses around a hypothetical salt diapir (Nikolinakou et al., 2014). Finally, 3D geomechanical models of salt structures were deemed useful to map out 3D stress fields around diapirs with multiple shapes (van-der-Zee et al., 2011). However, despite all this published work, fault or fracture analyses based on seismic-reflection or outcrop data have been sparsely used to reveal the palaeostress state around salt diapirs, though these approaches may provide more objective results (Quintà et al., 2012; Carruthers et al., 2013). Seismic interpretative work has so far been focused on understanding the stress state around circular or sub-circular salt diapirs (e.g. Carruthers et al., 2013). Their study focused on two small adjoining salt stocks, each one 2–3 km in diameter. In nature, many salt diapirs are larger than those in Carruthers et al. (2013) and show irregular shapes, so little is known about the palaeostress state surrounding the great majority of salt diapirs that are not small or concentric in their shape.

Salt diapirs formed in the Dutch North Sea are often surrounded by laterally extensive polygonal fault systems in Cenozoic claystone and shale (Cartwright, 2011; Carruthers et al., 2013). Polygonal faults are regarded as non-tectonic faults formed by the volumetric contraction of very fine-grained sediments that compact and dewater during their initial burial (Cartwright and Lonergan, 1996; Cartwright et al., 2003). Yet, abrupt changes from a typical polygonal fault pattern to arrays of radial faults are observed around the flanks of diapirs (Davison et al., 2000b; Stewart, 2006, 2007; Carruthers et al., 2013). These radial faults are formed by the circumferential stretching of strata when the salt diapirs grow (Jackson et al., 1994; Stewart, 2006; Yin and Groshong, 2007) or via stock widening ('stem push'), a mechanism capable of reactivating pre-existing radial faults or forming new ones under changing stress conditions (Coleman et al., 2018). Faults developed around salt diapirs are therefore capable of providing a relatively accurate record of the stress states associated with halokinesis (Quintà et al., 2012; Carruthers et al., 2013; Coleman et al., 2018).

Carruthers et al. (2013) mapped the geometry of polygonal fault patterns to reconstruct the evolving stress state of two salt diapirs in the UK Central Graben. Their work was based on the conclusion that polygonal faults are sensitive to local perturbations in horizontal stresses. Two possible mechanisms were thus proposed to explain the position of radial-polygonal fault boundaries: (1) the cessation of stretching caused by arching during diapir rise (Davison et al., 2000b; Carruthers et al., 2013), or (2) the limit of hoop stresses produced by radial loading of the overburden from a pressurised salt stock (Carruthers et al., 2013).

This work investigates the palaeostress state around a large triangular salt diapir in plan view, approximately 12.5 km wide, surrounded by polygonal faults. All seismically resolved faults (10,401 in total) were manually mapped around this salt diapir using high-quality 3D seismic data. Stress inversions were then applied to reveal the palaeostress state around the diapir of interest. This work provides insights into the evolving stress state around large, rising salt diapirs, an approach with implications to the analysis of salt structures and their adjacent strata in areas posed for carbon, hydrogen and natural gas storage, as well as the production of subsurface oil and gas. In summary, this work addresses the following research questions:

a) What is the structural evolution of irregularly shaped salt structures?
b) How does halokinesis control the formation and development of the fault families surrounding the salt diapir of interest?
c) What are the differences in stress state amongst the different zones surrounding irregularly shaped salt diapirs?

2. Geological setting

The Cleaver Bank High is an important gas producing area in the Southern North Sea (Fig. 1a). It spans an area of ~8000 km^2 and is bounded by the Broad Fourteens Basin to the south (Quirk, 1993) (Fig. 1b). The Cleaver Bank High was first developed in a Variscan foreland basin due to Permo-Carboniferous wrench tectonics and later recorded multiple tectonic episodes (Ziegler, 1990). These include a) Saalian tectonic uplift and erosion near the Late Carboniferous-Permian boundary, b) Late Permian-Early Jurassic extension and subsidence, c) Mid and Late Kimmerian erosion and continental rifting in the Middle and Late Jurassic, and d) Pyrenean and Savian tectonic inversion in the Middle to Late Paleogene (Fattah et al., 2012) (Fig. 3).

2.1. Upper paleozoic

During the Carboniferous, the Cleaver Bank High was located in the foreland basin of the Variscan orogen and became the locus of important sedimentation (Ziegler, 1990; Wong et al., 2007). Tectonic subsidence on the edges of the Variscan orogen was soon after followed by regional thermal uplift and igneous underplating, resulting in the erosion of Upper Carboniferous strata during the Saalian tectonic phase (Fattah et al. (2012). In some areas of the Southern North Sea, more than 1000 m of the Carboniferous Coal Measures were eroded below a regional Base Permian Unconformity (Quirk, 1993).

Following Saalian uplift and erosion, thermal relaxation and regional subsidence predominated in the Late Permian during which a succession of aeolian, fluvial sediments and desert-lake units were deposited as part of the Upper Rotliegend Group (Van Wees et al., 2000; Doornenbal and Stevenson, 2010). The Rotliegend strata were subsequently covered by evaporites, carbonates and clays of the Zechstein Group within a tectonic setting dominated by Late Permian-Triassic extension and subsidence (Fattah et al., 2012). The Zechstein Group includes sediments in repetitive cycles (Z1-Z5 in the Netherlands), which were controlled by the interplay between marine transgressions from the Arctic and evaporation of seawater in the arid Southern Permian Basin (Taylor, 1998; Peryt et al., 2010). The Z1-Z3 cycles comprise a typical evaporite sequence with, from bottom to top, claystone, carbonate, gypsum (and anhydrite), halite, potassium and magnesium salts. In turn, the Z4 and Z5 cycles comprise basal claystone and thin anhydrite or salt layers stratigraphically placed higher up in the sequence (Ten Veen et al., 2012). The thickest halite layers occur in the Z2 cycle (Strassfurt Halite Mb.) and Z3 cycle (Leine Halite Mb.), and their thickness was originally ~650 m based on structural restorations published in Ten Veen et al. (2012).

2.2. Mesozoic

Deposition on the Cleaver Bank High continued into the Jurassic, once again preceding thermal doming and the subsequent tectonic uplift of the study area in the Middle and Late Jurassic (Ziegler, 1990; Wong et al., 2007). This younger phase of tectonic uplift related to continental rifting and associated fall in sea level, and resulted in widespread erosion of structural highs in the Southern North Sea; the so-called Mid and Late Kimmerian tectonic phases (Ziegler, 1990; Wong et al., 2007; Ten Veen et al., 2012). Consequently, Upper Triassic and Lower Jurassic strata are completely absent on the Cleaver Bank High (Quirk, 1993).

Sea level rose during the Early Cretaceous and gradually flooded the study area (Fattah et al., 2012). For this reason, siliciclastic deposits overlie Triassic strata and, locally, the Zechstein Group. Regional

thermal subsidence prevailed in the Late Cretaceous and a thick succession of limestones (Chalk Group) was subsequently deposited (Fattah et al., 2012). At the same time, the Alpine orogeny was initiated in Central Europe due to convergence of the African and the Arabian plates with Eurasia. The eastern Tethys Ocean was closed in the Late Cretaceous, accompanying tectonic inversion in central Europe (Wong et al., 2007; Fattah et al., 2012). Nevertheless, the Cleaver Bank High was not significantly affected by tectonic inversion during the Late Cretaceous Sub-Hercynian phase, as the Chalk Group shows a relatively uniform thickness in seismic profiles (Chen, 2016).

2.3. Cenozoic

Cenozoic sediments unconformably overlie the Chalk Group on the Cleaver Bank High (Figs. 5–8). They consist of clays, silts, fine-coarse grained sands. Two important inversion episodes affected the study area during the Paleogene, the Pyrenean (Middle Paleogene) and Savian (Late Paleogene) tectonic phases. Apatite fission-track data have shown that the Cleaver Bank High was uplifted during Pyrenean inversion (Alberts et al., 1991). In contrast, Savian tectonic inversion is only marked by a stratigraphic unconformity between Paleogene and Neogene strata documenting a brief depositional hiatus (Chen, 2016).

Halokinesis was important on the Cleaver Bank High, resulting in the formation of salt structures at its edge, especially salt pillows and diapirs (Remmelts, 1995; Ten Veen et al., 2012). Importantly, most of these salt structures are oriented NW-SE and follow the strike of basement faults. Halokinesis is much more pronounced in the northeast sector of this high (Remmelts, 1995).
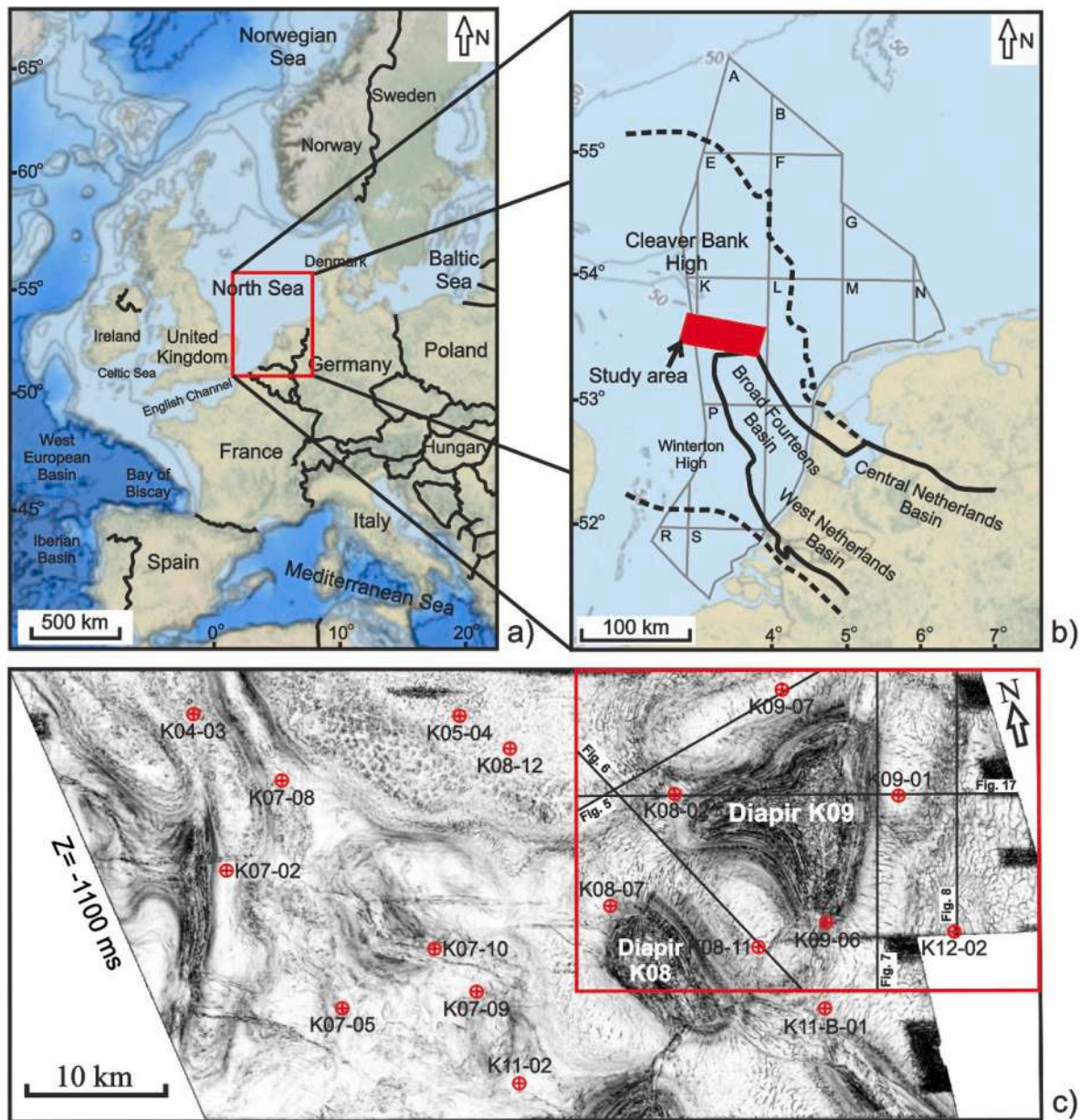
Fig. 1. a) Bathymetric map of NW Europe and its continental margin. The red polygon shows the location of Fig. 1b. b) Bathymetric map showing the position of the Dutch sector of the Southern North Sea, which is bounded by the grey polygon. The Broad Fourteens Basin, Central Netherlands Basin and West Netherlands Basin are highlighted by a black solid line, whereas the Cleaver Bank and Winterton highs are highlighted by a black dash line. The red rectangle shows the location of the 3D seismic volume. Bathymetric map is taken from the National Centre for Environmental Information. c) Variance map (Z=−1100 ms two-way time) highlighting the location of study area by a red polygon. Boreholes are shown by their common symbol; a red cross and circle. The seismic profiles shown in Figs. 5–8 and 17 are shown by the black lines.

Salt movement started between the Middle Triassic and Early Cretaceous, with precise estimates being hampered by broad depositional hiatuses in the Mesozoic sedimentary record (Remmelts, 1995). Further salt movement occurred during the Late Cretaceous and Eocene-Oligocene, accompanying tectonic inversion (Glennie, 1997; Harding and Huuse, 2015; Deckers et al., 2022). Major fold structures cored by salt pillows were initiated or amplified during these multiple tectonic phases (Stewart and Coward, 1995; Stewart, 2007; Harding and Huuse, 2015; Hernandez et al., 2018).

3. Data and methods

This work uses three-dimensional (3D) seismic data from the Southern North Sea (Figs. 1 and 2). The seismic data were acquired in the southern end of the Cleaver Bank High between 53.35° and 53.76°N and 3.81°-3.95°E, and cover an area of around 2120 km² (Fig. 1b). The seismic data comprise a 22 × 32 km rectangular survey acquired at an average water depth of 35 m (Figs. 1 and 2). The seismic data are zero-phased and displayed using the European SEG polarity convention in which an increase in acoustic impedance is shown as a red seismic reflection, while a decrease in impedance is shown as a black seismic reflection. Inline and crossline spacings are 25 m, and data were processed with a 25 × 25 m bin size. The dominant seismic frequency in Cenozoic strata is 50 Hz, resulting in a vertical resolution ranging from 8 to 12 m for 1/4 of the wavelet frequency, or λ/4. In addition, seven wells drilled near the diapir of interest to this study provide Gamma Ray (GR), Lithology, Density (RHOB) and Sonic (DT) data. These seven wells are tied to the seismic volume using their checkshot data. Well correlations are completed in this work to identify lithological variations and establish a chronostratigraphic framework for the interpreted seismic-stratigraphic units (Figs. 3 and 4).

In this work, eight (8) key seismic-stratigraphic horizons are interpreted and correlated with borehole data (Figs. 5 and 6), revealing the main chronostratigraphic framework of the study area. Seven other seismic horizons are interpreted within the Lower North Sea Group (Figs. 5–8). In addition, graphs recording the number of faults offsetting the interpreted seismic horizons are compiled to identify tier boundaries in polygonal fault systems (Figs. 5–8). This is because polygonal fault tiers are generally identified by comparing the polygonal planforms of faults at different horizons and by analysing the clustering of basal and upper fault tips at specific horizons (Cartwright and Lonergan, 1996; Carruthers et al., 2013). Thus, plots of the number of faults intersecting each seismic horizon are useful to identify the positions of each tier and their respective boundaries (Carruthers et al., 2013). Three principal seismic-stratigraphic units are defined in Cenozoic strata based on the tier boundaries of polygonal fault systems (horizon H5) and regional stratigraphic unconformities (horizon H9). Isochron maps for these three seismic-stratigraphic units, and the Late Cretaceous Chalk Group, are plotted to understand the growth history of the salt diapir of interest to this study.

The study area comprises a large triangular salt diapir, in plan view, that bounds gas field K09-ab-B to the west. To this diapir is given the name diapir K09 based on the quadrant of the Southern North Sea in which it mostly occurs (Fig. 1). Diapir K09 is surrounded by three salt withdrawal basins along its three distinct flanks (Fig. 1c and 2). Radial faults are well developed near diapir K09, with polygonal and keystone faults developed further away from this structure (Fig. 2). Variance time-slices were used to identify the fault families developed around diapir K09 (Figs. 1–2), as they are imaged as sharp discontinuities in such seismic attribute data (Brown, 2011).

A total of 10,401 faults were manually interpreted every two cross-lines/inline (50 m) around this same diapir (See Supplementary File 1). Fault-point data were obtained by discretising the faults interpreted on Petrel® into facets, and time-depth conversions were applied to these
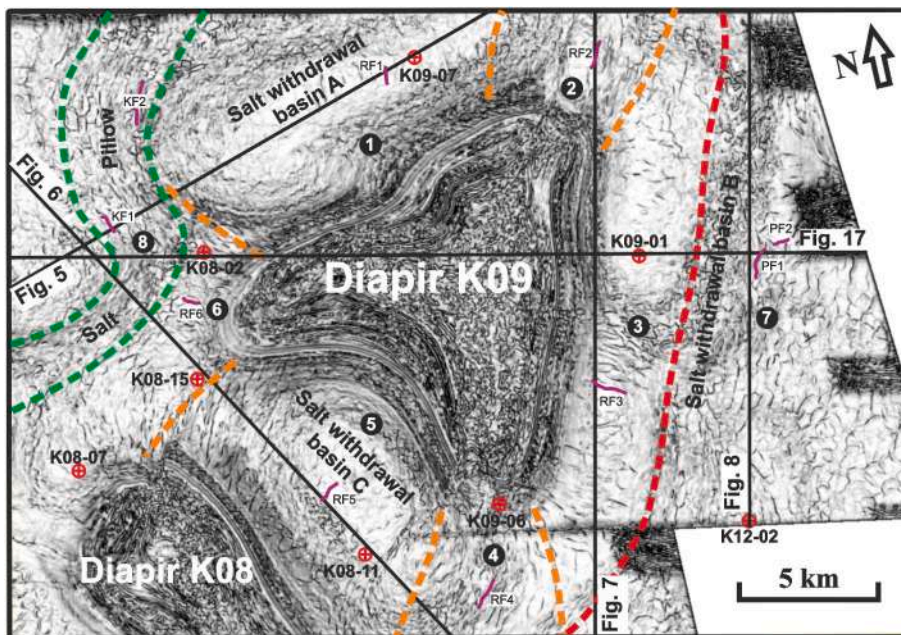

Fig. 2. Variance time-slice (Z=−1100 ms two-way time) of the study area highlighting eight zones and salt structures interpreted in this work. Six flanking and corner zones are separated by orange dash lines and labelled 1 to 6. Zones where polygonal and keystone faults were developed are bounded by red or green lines, which are respectively labelled 7 and 8. Boreholes are shown by a red cross and circle. The seismic profiles shown in Figs. 5–8 and 17 are shown by black lines. Ten faults in total from eight zones, shown with purple lines, were selected for throw-length (T$_{max}$-L) and throw-depth (T–Z) analyses (see Figs. 12–14).
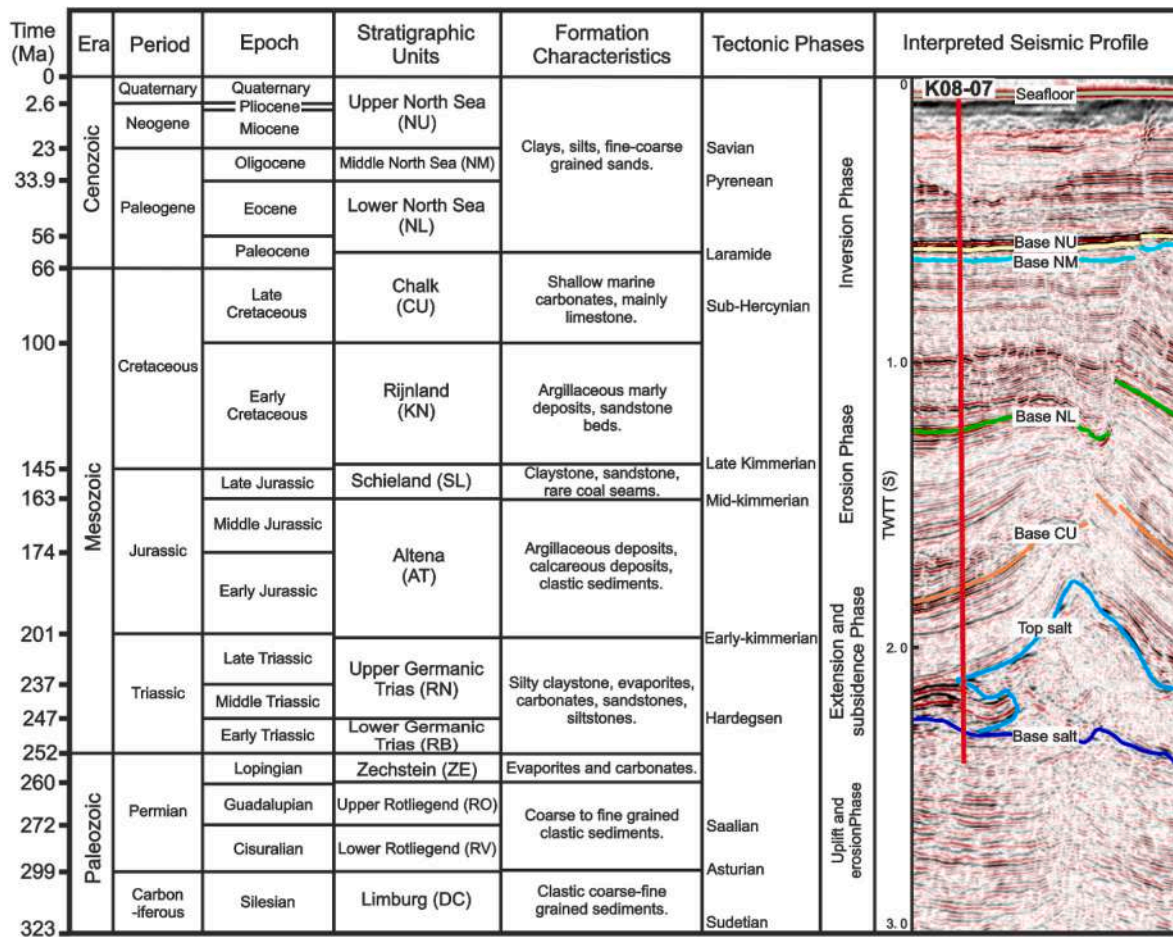
Fig. 3. Tectono-stratigraphic chart for the Cleaver Bank High showing main stratigraphic units and formation characteristics (modified from Harding and Huuse, 2015). Multiple tectonic events and four tectonic evolutionary phases are highlighted in the figure. Important seismic-stratigraphic horizons, correlated with data from well K08-07, are shown in the seismic profile.

same facets on Move®. Rose diagrams representing the distribution of fault strikes for each zone were plotted using fault-point data on Move®; the radius value of the rose diagrams is plotted as a ratio. The mapped faults were used to identify eight zones based on their geometry, strike and overall distribution (Fig. 2; Table 1). Additionally, ten faults from the eight zones were selected to compile throw-length (T_{max}-L) and throw-depth (T-Z) plots, which were later used to study the faults' growth history (Figs. 12–14; Watterson, 1986; Walsh and Watterson, 1988; Cowie and Scholz, 1992; Kim and Sanderson, 2005; Omosanya et al., 2015; Omosanya, 2020). Importantly, we used the criteria of Tao and Alves (2019) to record throw data for distinct fault segments. Tao and Alves (2019) proposed that minimum throw/displacement sampling intervals are related to the length of a fault; sampling intervals should be less than 5% of the fault length when the latter is < 3500 m, or 3% of the fault length when this length is > 3500 m.

Stress inversions are applied in this work to estimate palaeostress tensors from faults interpreted in each zone. Such a method relies on the basic assumption that slip on each fault plane occurs in the direction of maximum resolved regional shear stress (Pollard et al., 1993), and was completed using the Stress Analysis Module on Move®. This module is based on the direct inversion method of Angelier (1990) and uses dip-slip data of the interpreted faults from each zone, including dip and dip azimuth. We therefore estimated the orientation and distribution of palaeostress tensors responsible for the formation of faults in the study area (Table 2). Additionally, ant tracking maps were compiled to highlight changes in the width of flanking and corner zones around salt diapir K09. Dip maps for four key horizons were plotted to compare flanking with corner zones.

4. Seismic stratigraphic units

4.1. Unit 1 (horizons H0 to H5)

Unit 1 consists of a package with low-to moderate-amplitude internal seismic reflections (Figs. 5–8). It is bounded at its base by horizon H0 (or Base NL, Lower North Sea Group), a high-amplitude reflector that
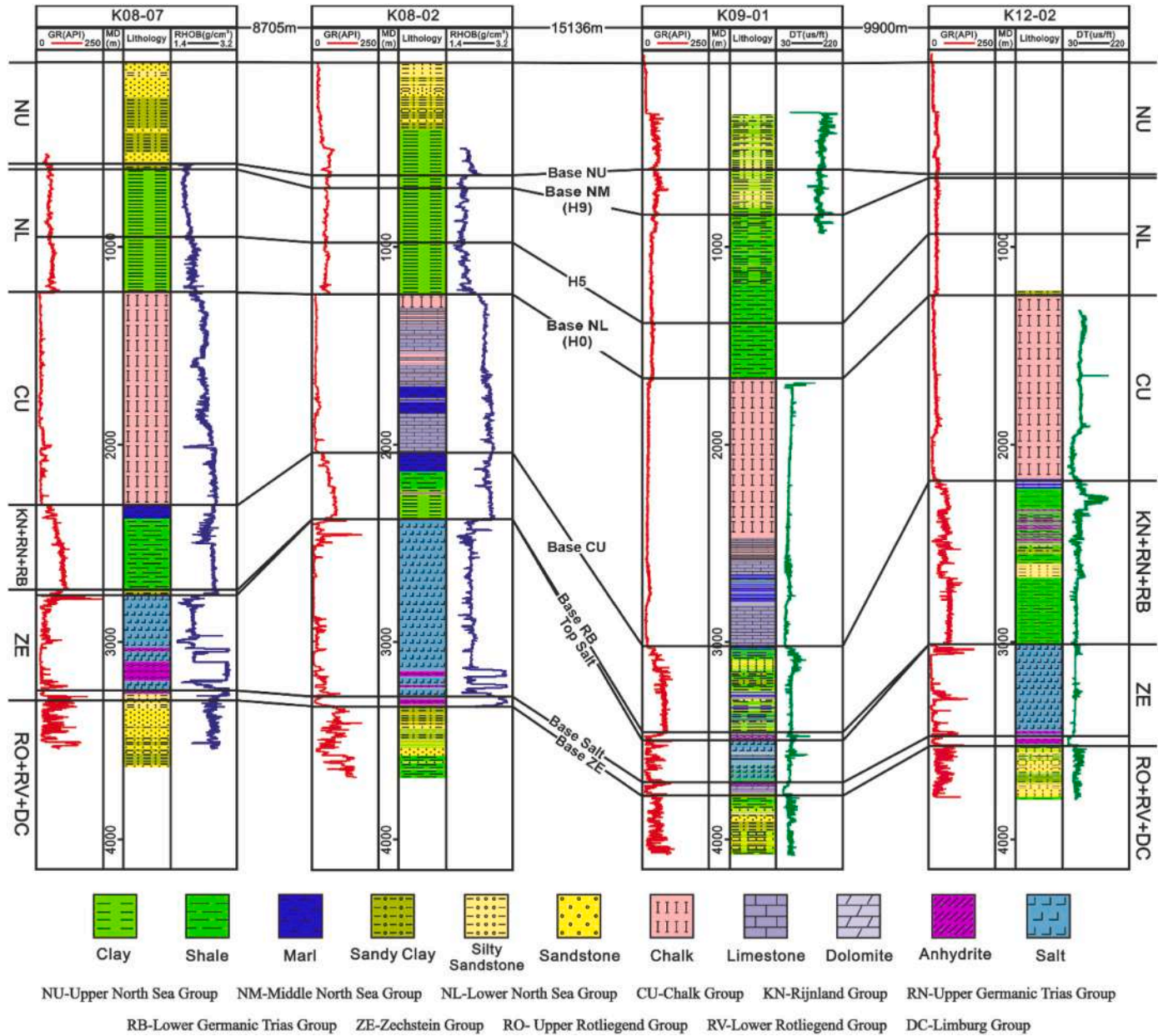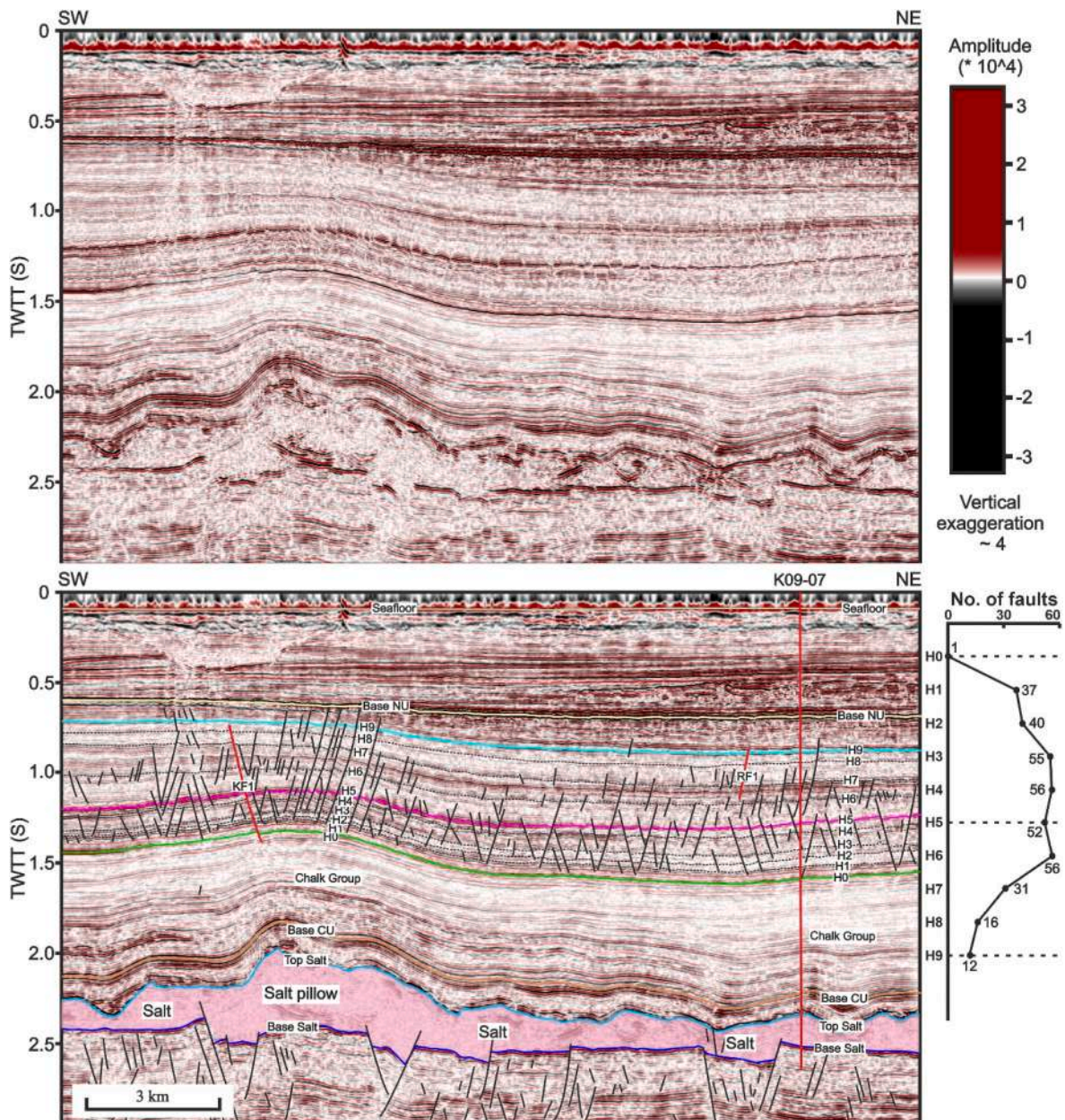
Fig. 4. Stratigraphic correlation for wells K08–07, K08–02, K09–01 and K12-02 drilled in the study area. Stratigraphic framework, lithology, gamma-ray (GR), density (RHOB) and sonic log (DT) wireline curves are shown in the figure.

Fig. 5. Seismic profile across the salt pillow and salt withdrawal basin A highlighting the presence of keystone faults and radial faults. Eight seismic horizons correlated with well K09-07 are shown by lines and labels with different colours, whereas seven other horizons are shown by black dash lines and labels. Faults are represented by black or red lines, including keystone fault 1 (KF1) and radial fault 1 (RF1). Well (K09-07) is shown by a red bold line. The graph to the right of the seismic section highlights the number of faults crossing distinct seismic-stratigraphic horizons. The location of the seismic profile is shown in Fig. 2. CU-Chalk Group.

correlates with the base of Paleogene strata. Its top is bounded by a moderate-to high-amplitude reflector named horizon H5 (Figs. 5–8). The thickness of Unit 1 varies between 20 and 470 ms, with strata in the eastern part of the study area being thicker than in the west (Figs. 5 and 6). In addition, four seismic reflections were interpreted between horizons H0 and H5, and divide Unit 1 into five different sub-units (Figs. 5–8).

Unit 1 is composed of clay and shale with moderate gamma-ray values (~50 API), but low-density values (~1.9 g/cm^3) (Fig. 4). Faults are common inside Unit 1 but rarely propagate below its base (Figs. 5–8). This is because the underlying Chalk Group is composed of chalk and other carbonate rocks that are relatively hard (Rafavich et al., 1984; Ferrill and Morris, 2008; Ferrill et al., 2017). Conversely, there are multiple faults propagating upwards into Unit 2 (Figs. 5–8).

4.2. Unit 2 (horizons H5 to H9)

Unit 2 is bounded at its base by horizon H5 and at its top by horizon H9 (or Base NM, Middle North Sea Group), a low-to moderate-amplitude reflector that correlates with the base of the Middle North Sea Group (Figs. 5–8). Three seismic reflections are interpreted between horizon H5 and H9, dividing Unit 2 into sub-units, 2a to 2d. Sub-units 2a, 2c and 2d consist of distinct low amplitude or transparent seismic reflections, whereas sub-unit 2b includes a package of moderate-to high-amplitude seismic reflections (Figs. 5–8). The thickness of the entire Unit 2 varies from 87 to 540 ms, decreasing towards the flanks of diapir K09 (Fig. 10). Unit 2 is also composed of clay and shale with moderate gamma-ray (~50 API) and low density values (~2.0 g/cm^3) (Fig. 4). Faulting is ubiquitous in this interval; although a few faults propagate upwards into Unit 3, most faults terminate near horizon H9 (Figs. 5–8).
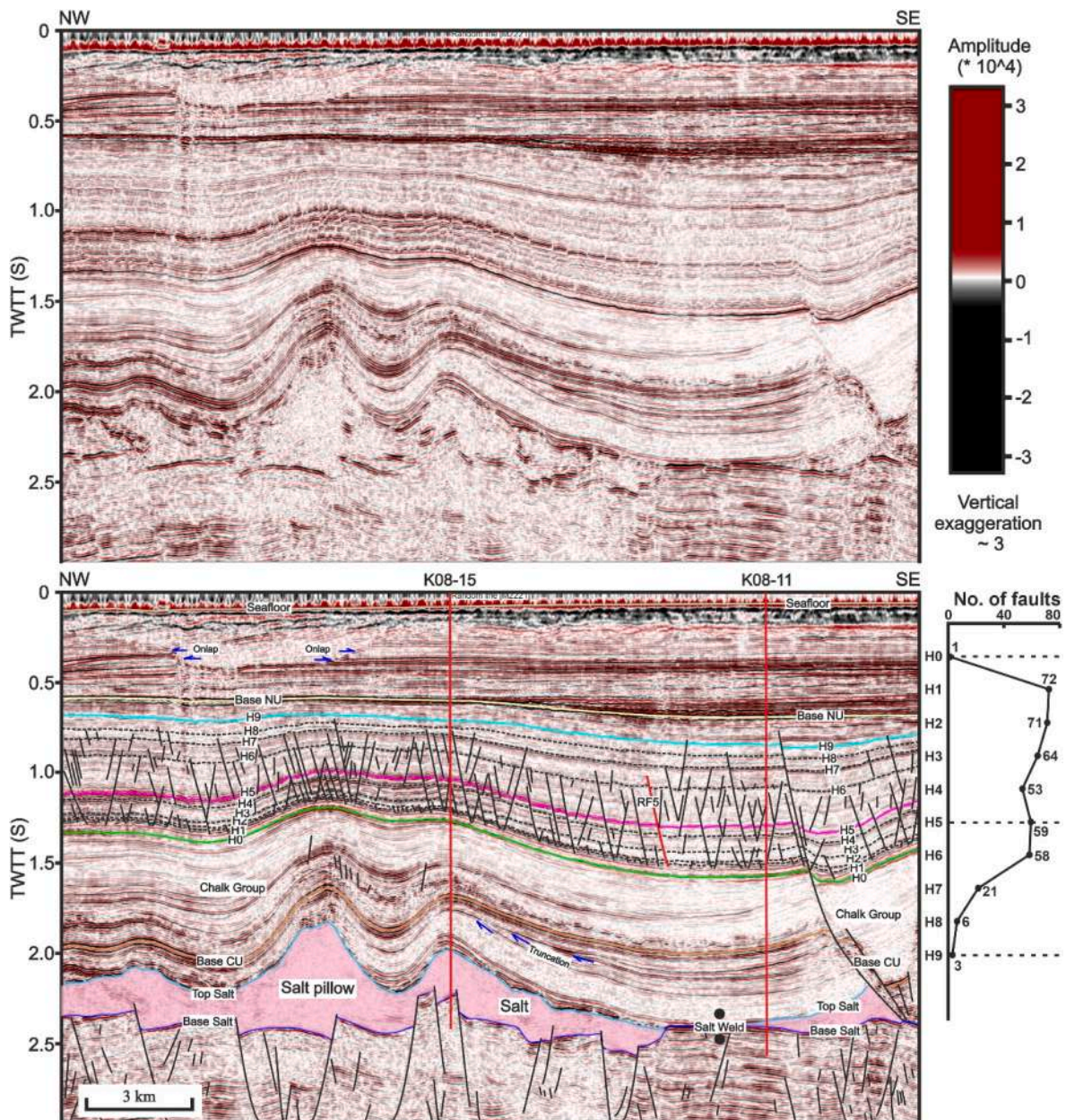
Fig. 6. Seismic profile across the salt pillow and salt withdrawal basin C highlighting the presence of keystone and radial faults. Eight seismic horizons correlated with wells K08–15 and K08-11 are shown by lines and labels with different colours, whereas seven other horizons are shown by black dash lines and labels. Faults are represented by black or red lines, including radial fault 5 (RF5). Wells K08–15 and K08-11 are shown by red bold lines. A salt weld is highlighted by two black circles. The graph to the right of the seismic section shows the number of faults cross-cutting distinct seismic-stratigraphic horizons. The location of the seismic profile is shown in Fig. 2. CU-Chalk Group.

4.3. Unit 3 (horizon H9 to the seafloor)

The base of Unit 3 coincides with horizon H9, whereas its top is delimited by the seafloor (Figs. 5–8). Its thickness ranges from 470 to 860 ms, comprising an interval with moderate-to high-amplitude seismic reflections (Figs. 5–8). Unit 3 correlates with the Middle and Upper North Sea groups, which are separated by horizon Base NU (Figs. 5–8). Unit 3 is composed of clay, sandy clay, silty sandstone and sandstone, recording gamma-ray values of ~60 API in its lower part and low gamma-ray values (~25 API) at its upper part (Fig. 4). A few faults are developed in the Middle North Sea Group, between horizons H9 and NU, but are rarely observed between horizon NU and the seafloor (Upper North Sea Group) (Figs. 5–8).

5. Salt structures and surrounding fault families

5.1. Geometry of salt structures

Diapir K09 is a large triangular diapir in plan view, spanning an area of around 95 km^2 at a depth of ~1100 ms two-way time (Fig. 2). It penetrates Triassic to Holocene strata overlying large basement faults (Fig. 17). Diapir K09 is surrounded by three salt-withdrawal basins along its north, east and southwest flanks; respectively basins A, B and C (Fig. 2). In this same area, diapir K09 is separated from basin B by a large NE-striking Mesozoic fault crossing the entire seismic volume (Fig. 6), as also shown in Fig. 1 of Ten Veen et al. (2012).

Basins A to C were mainly developed in the Paleogene, as marked thickening occurs in the Lower North Sea Group between horizons H0
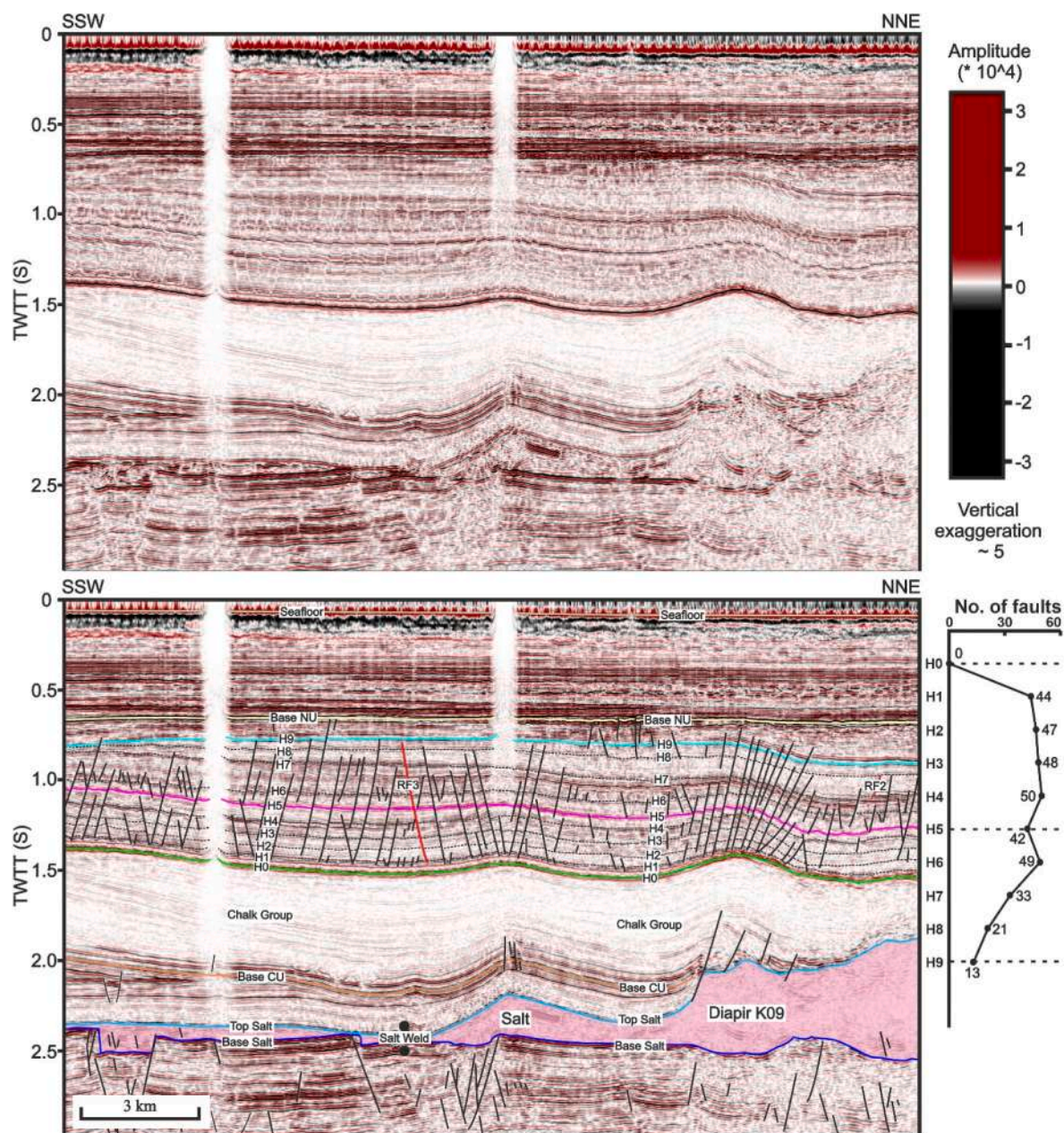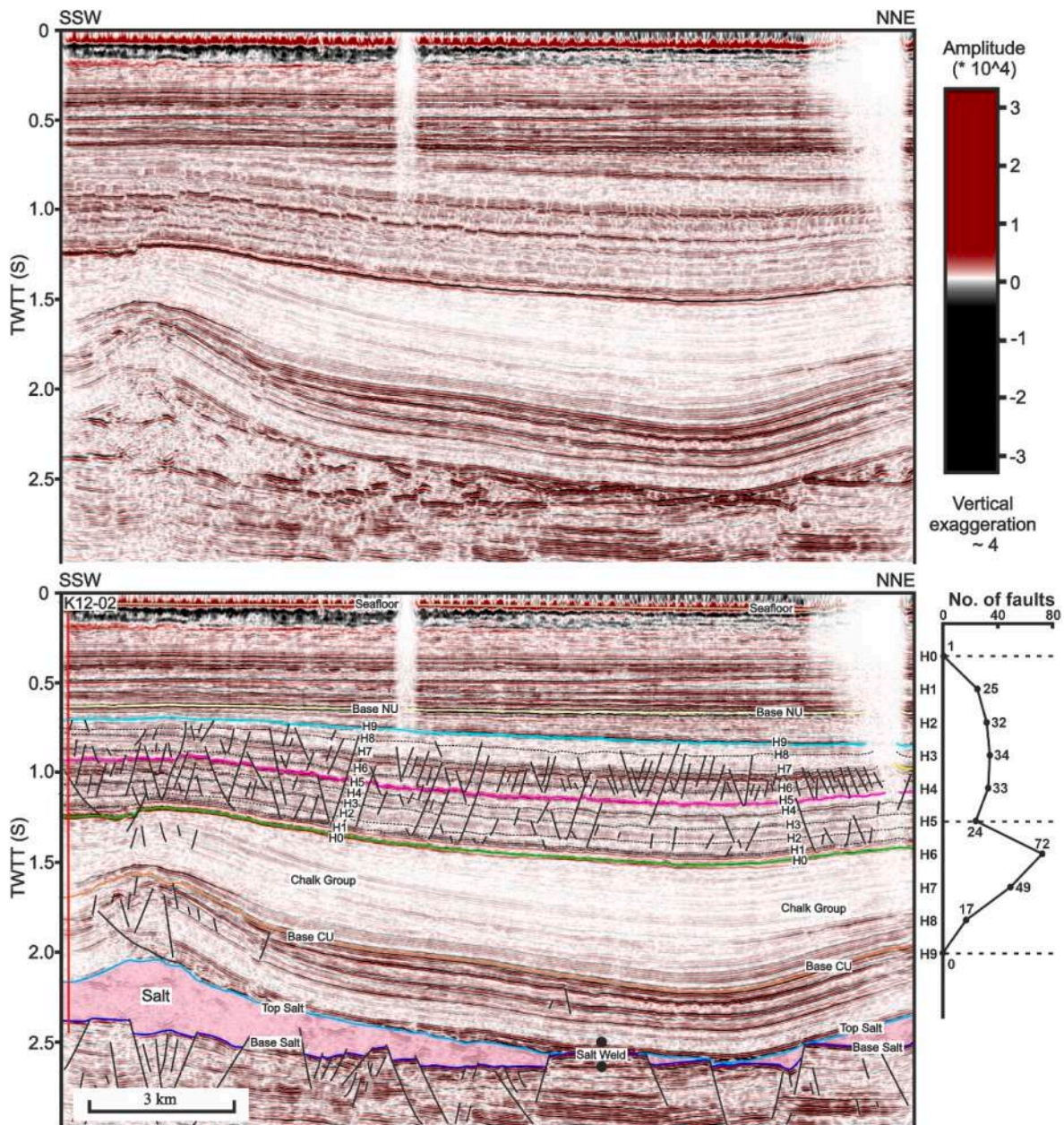
Fig. 7. Seismic profile across salt withdrawal basin B highlighting the presence of radial faults. Eight seismic horizons are shown by lines and labels with different colours, whereas seven other horizons are shown by black dash lines and labels. Faults are represented by black or red lines, including radial fault 3 (RF3). A salt weld is highlighted by two black circles. The graph to the right of the seismic section shows the number of faults cross-cutting distinct seismic-stratigraphic horizons. The location of the seismic profile is shown in Fig. 2. CU-Chalk Group.

and H9 (Fig. 10). In seismic data, salt welds are observed below these basins (Figs. 6–8). In addition, basin B is wider than basins A and C, partly because the two latter are limited by other salt structures, not only by diapir K09 (Figs. 9 and 10). For instance, basin C is also bounded by the relatively large diapir K08 to the west, while a S-shape salt pillow developed near the northwest flank of diapir K09, covering an area of around 38 km² at the depth of −1100 ms two-way time (Fig. 2).

5.2. Fault families developed around diapir K09

Faults developed near diapir K09 include radial, polygonal and keystone faults (Figs. 2 and 9). Eight (8) distinct zones are recognised based on the geometry, strike and distribution of such faults (Fig. 2). Flanking zones concern the areas where radial faults are developed along the flanks of diapir K09, with these faults showing similar strikes, particularly in zones 1, 3 and 5, with average orientations of N182, N107

Fig. 8. Seismic profile across salt withdrawal basin B showing polygonal faults. Eight seismic horizons correlated with well K12-02 are shown by lines and labels with different colours, whereas seven other horizons are shown by black dash lines and labels. Faults are represented by black lines. Well K12-02 is shown by a red bold line. A salt weld is shown by two black circles. The graph to the right of the seismic section shows the number of faults cross-cutting distinct seismic-stratigraphic horizons. The location of the seismic profile is shown in Fig. 2. CU-Chalk Group.

and N63 (Figs. 2 and 9). Comparatively, corner zones comprise radial faults developed around the corners of diapir K09 (Figs. 2 and 9). The strike of these radial faults varies as one travels from one flank to the other, along the diapir corners, as in zones 2, 4 and 6 (Fig. 2). In addition, polygonal faults were developed in zone 7, next to flanking zone 3 (Figs. 2 and 9). Keystone faults were formed in zone 8 above the salt pillow, with strikes parallel to this latter (Figs. 2 and 9).

5.2.1. Radial faults

Radial faults are well developed in the vicinity of diapir K09 (Figs. 2 and 9). In plan view, their distribution and number show significant differences with depth, a character associated with the growth history of diapir K09 itself (Fig. 9). For example, radial faults occur over a wider area at horizons H3, H5 and H7 when compared to horizon H1 (Fig. 9). Their spacing at the level of horizons H3, H5 and H7 is also broader than

at horizon H1 (Fig. 9). Importantly, the strike and number of radial faults vary in distinct zones (Fig. 9; Table 1). The strike of radial faults in flanking zones are clearly oriented when compared with the variably striking of radial faults in corner zones. Radial faults are near-normal to the flank of diapir K09 in flanking zones, whereas they are roughly parallel to the direction of its corner bisector in corner zones (Fig. 11). Furthermore, the number of flanking radial faults is usually greater than corner radial faults (Table 1).

In seismic data, most radial faults are similar to polygonal faults, i.e., they are restricted to shale or clay intervals in the Lower North Sea Group (Figs. 4–8). However, plots of the number of radial faults at each seismic horizon show important differences when compared to polygonal faults (Figs. 5–8). In the study area, radial faults are not tier bounded as polygonal faults are. Radial faults have also different length, throw and spacing values when compared to polygonal faults. The

Table 1

Summary of fault attributes compiled within the eight zones developed around salt diapir K09.

Faults in eight zones	Number of faults	Main Strike	Mean strike	Mean dip	Dip range
Radial faults in flanking zone 1	938	N–S	181.7	56.1	47.4–65.4
Radial faults in corner zone 2	201	SW-NE	136.4	55.5	47.6–65.2
Radial faults in flanking zone 3	1248	NW-SE	107.0	57.9	51.1–66.3
Radial faults in corner zone 4	226	SW-NE	355.1	56.7	46.2–66.9
Radial faults in flanking zone 5	445	SW-NE	62.6	52.8	47.3–68.1
Radial faults in corner zone 6	192	NW-SE	165.0	54.7	46.3–65.0
Polygonal faults (Tier 1) in zone 7	4788	SW-NE	58.4	56.0	48.4–65.2
Polygonal faults (Tier 2) in zone 7	1571	SW-NE	61.4	54.7	47.3–64.3
Keystone faults in zone 8	792	SW-NE	152.8	53.3	45.8–63.3

Table 2

Principal palaeostress tensors obtained from stress inversions in the eight zones developed around salt diapir K09. Results show σ_1 is nearly vertical, whereas σ_2 and σ_2 are sub-horizontal.

Faults in eight zones	σ_1		σ_2		σ_3	
	Plunge	Azimuth	Plunge	Azimuth	Plunge	Azimuth
Radial faults in flanking zone 1	−87.4	89.6	0.2	174.4	2.6	84.4
Radial faults in corner zone 2	87.9	51.9	−2.0	33.2	−0.7	123.2
Radial faults in flanking zone 3	−86.0	199.7	−0.8	301.0	−4.0	31.1
Radial faults in corner zone 4	87.8	183.5	2.0	30.6	−1.0	120.5
Radial faults in flanking zone 5	−84.2	136.9	0.6	53.3	5.8	143.3
Radial faults in corner zone 6	−88.6	103.6	1.4	114.6	−0.3	204.6
Polygonal faults (Tier 1) in zone 7	88.3	356.9	−1.4	29.6	0.9	119.6
Polygonal faults (Tier 2) in zone 7	88.5	8.0	−1.4	28.4	0.5	118.3
Keystone faults in zone 8	88.9	358.4	−1.0	20.8	0.4	110.8

length of radial faults ranges from 400 to 3500 m, and throws vary from 9 to 45 m. The spacing of radial faults varies from 10 to 140 m, values that are larger than those of polygonal faults (Fig. 9).

Six radial faults were selected to compile throw-length (T_{max}-L) and throw-depth (T-Z) plots; radial fault 1 (RF1) to radial fault 6 (RF6) (Fig. 12). RF1, RF3 and RF5 are 800, 2080 and 1020 m long, respectively dipping to the W, NNE, and SE (Fig. 2). RF1 was formed by the lateral propagation and linkage of fault segments, as distinct throw minima are shown in the T_{max}-L plot in Fig. 12a. In contrast, RF3 and RF5 are isolated faults as shown by their rugged curve profiles, which reveal the highest throw near their centre but the lowest throw at their lateral tips (Fig. 12k–u). The maximum throw of RF1 occurs near horizon H5, while throw maxima for RF3 and RF5 occur around horizon H6. Multiple throw minima are observed on their T-Z plots, suggesting they were formed by dip linkage (Fig. 12).

Corner radial faults RF2, RF4 and RF6 are 1104, 1700 and 875 m long, dipping respectively to the SE, SE, and NNE (Fig. 2). RF2 is an isolated fault, showing a rugged curve profile that shows the highest throw near the centre position of RF2 but the lowest throw at both sides in T_{max}-L data (Fig. 12b). RF4 and RF6 were formed by the lateral propagation and linkage of fault segments, as distinct throw minima are shown in their T_{max}-L plots (Fig. 12l–v). The maximum throw of RF2 occurs near horizon H3, while throw maxima for RF2 and RF3 occur around horizon H6. Similarly to RF1, RF3 and RF5, multiple throw minima in T-Z plots suggest they were formed by dip linkage (Fig. 12).

5.2.2. Polygonal faults

Polygonal fault systems are typically characterised by their geometric planforms, and are often restricted to specific tiers (Cartwright, 1994). In the study area distinct polygonal planforms are observed in basin B within shale or clay intervals of the Lower North Sea Group (Figs. 2 and 9). The area occupied by the polygonal faults changes with depth (Figs. 9 and 16), reflecting variations in the span of radial faults during the rise of diapir K09. In addition, plots recording the number of faults intersecting each seismic horizon show minimum values (curve minima) in horizons H0, H5 and H9, whereas maximum values (curve

maxima) are recorded in horizons H3 and H6 (Fig. 8). This reveals the presence of two distinct polygonal fault tiers in the study area; Tier 1 occurs between horizons H0 and H5, while Tier 2 spans the interval between horizons H5 and H9 (Fig. 8). The boundary between Tiers 1 and 2 is located at horizon H5, where most faults tip out, though a few polygonal faults are linked across this same horizon (Fig. 8).

A total of 4,788 polygonal faults were interpreted in Tier 1, and 1,571 polygonal faults were interpreted in Tier 2 (Table 1). The thickness of Tiers 1 and 2 is around 500 and 450 m, respectively (Fig. 10). Polygonal faults in Tier 1 are shorter than those in Tier 2, ranging from 200 to 1200 m (Tier 1) to 350–1500 m (Tier 2). Fault throws in Tier 1 are similar to Tier 2, varying from 5 to 35 m. In parallel, polygonal faults in Tier 1 are formed closer than in Tier 2, with their spacing ranging from 140 to 400 m in Tier 1 and from 300 to 500 m in Tier 2. In addition, polygonal faults in Tiers 1 and 2 are aligned, although appearing to be randomly distributed on the structural maps in Fig. 9.

Polygonal faults in Tier 1 strike to the NE, mainly from N0 to N60, and their dips range from 48.4° to 65.2° (Fig. 11h; Table 1). Similarly, polygonal faults in Tier 2 also strike to the NE, mainly from N0 to N60, and their dips range from 47.3° to 64.3° (Fig. 11i; Table 1). This indicates that polygonal faults were influenced by the stress field surrounding diapir K09, which promoted their preferential alignment. However, this surrounding stress field did not significantly change when polygonal faults were formed as they show similar strikes across horizon H5 in both Tiers 1 and 2 (Fig. 11h–i).

Two polygonal faults were selected to compile throw-length (T_{max}-L) and throw-depth (T-Z) plots, polygonal fault 1 (PF1) and 2 (PF2) (Fig. 13). PF1 and PF2 are 1260 m and 830 m long, dipping respectively to the SE and NNE (Fig. 13). PF1 is an isolated fault, showing a rugged curve profile with its maximum throw value near the centre of PF1. Throw minima occur near its lateral tips, though its eastern half is intersected by another fault (Fig. 13a). PF2 grew via the lateral propagation and linkage of fault segments, as distinct throw minima occur in T_{max}-L data between the positions of profiles i and j (Fig. 13b). PF1 offsets strata between horizons H1 and H9, while PF2 offsets strata between horizons H1 and H7.
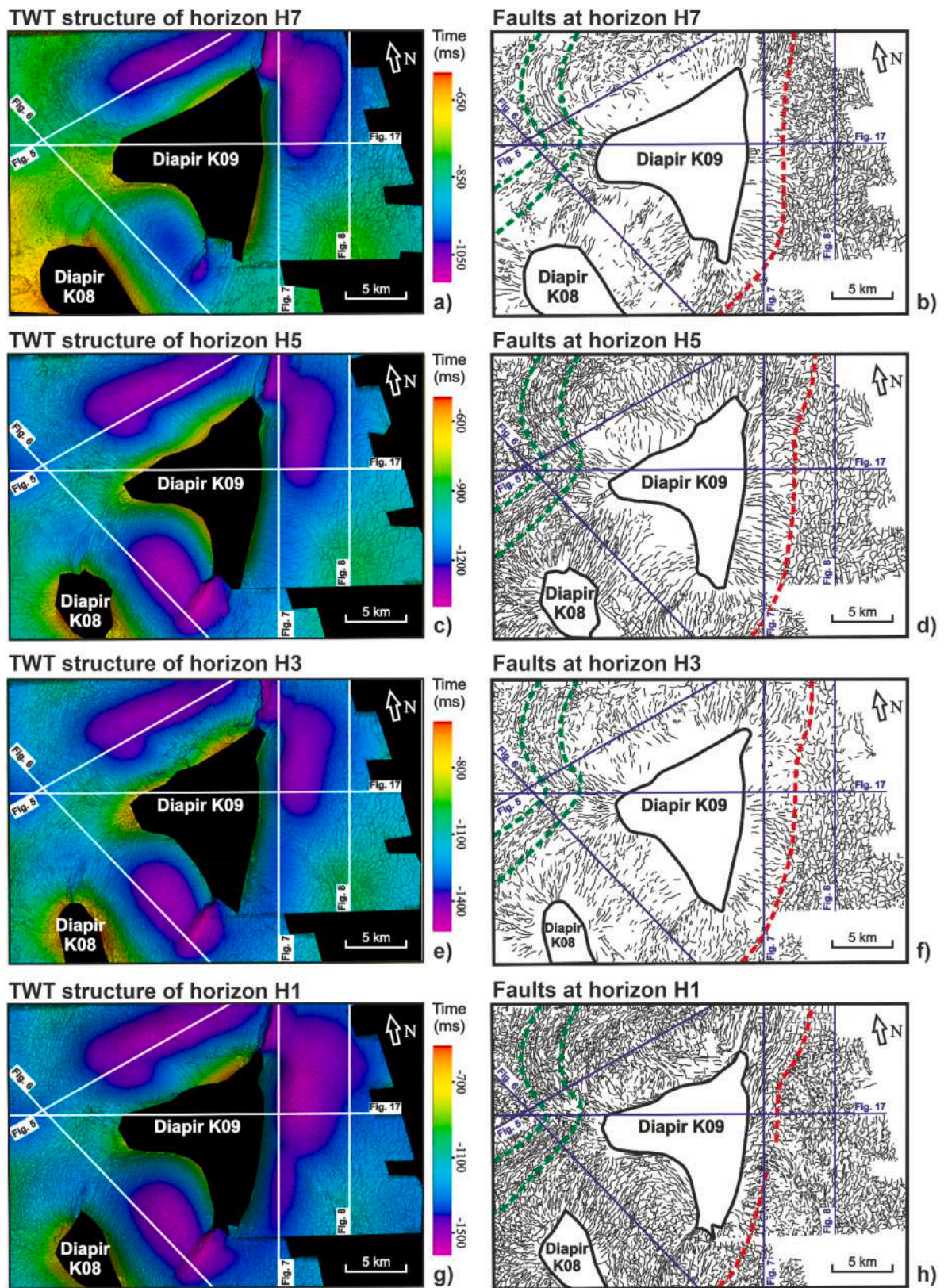
Fig. 9. TWT structural and fault maps for four key horizons in the study area highlighting the variation of faults at different horizons. a), c), e) and g) TWT structure of horizons H7, H5, H3 and H1, respectively. b), d), f) and h) Faults at horizons H7, H5, H3 and H1, respectively. Faults are shown by black lines in fault maps. Zones in which keystone faults were developed are bounded by green dash lines, whereas the zones where radial and polygonal faults were developed are separated by a red dash line. The seismic profiles in Figs. 5–8 and 17 are shown by white or blue lines.
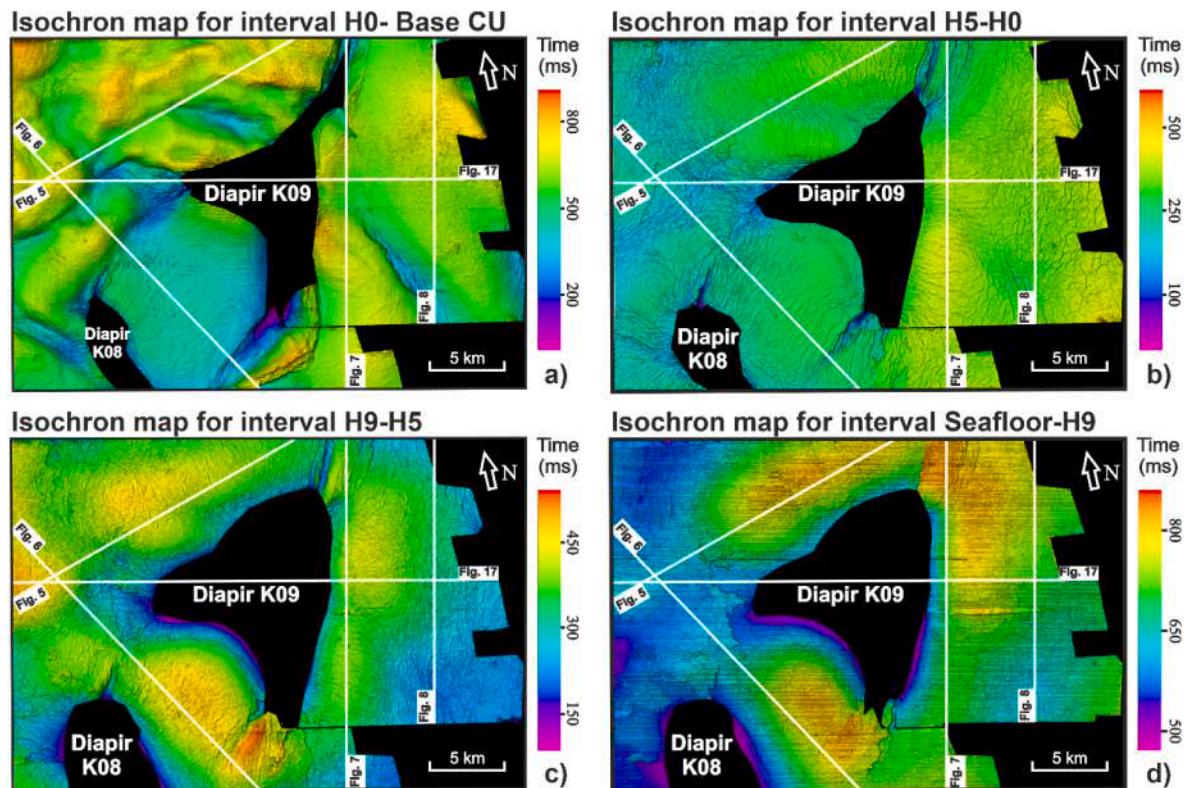
Fig. 10. Isochron maps for seismic intervals in the study area. a-d) Isochron maps for seismic intervals between horizon H0 and Base CU, between horizons H5 and H0, between horizons H9 and H5, and between the seafloor and horizon H9. The seismic profiles in Figs. 5–8 and 17 are shown by white lines. CU-Chalk Group.

Throw maxima in PF1 occur just below horizon H3, suggesting it probably first nucleated at this depth (Fig. 13). Interestingly, multiple throw minima are observed on the T-Z profiles of PF1 (Fig. 13c, d and 13e), suggesting it was formed by dip linkage. The throw maxima of PF2 occurs around horizon H4, indicating it nucleated around this horizon (Fig. 13). Multiple throw minima are also observed in T-Z data for PF2 (Fig. 13g–j), also suggesting it was formed by dip linkage. Throw minima occur around horizon H5, which separates Tiers 1 and 2 (Fig. 13d, e and 13j). This implies PF1 and PF2 were formed by the linkage of polygonal faults growing separately in both tiers.

5.2.3. Keystone faults

Keystone faults were developed above a salt pillow next to flanking zone 1 and corner zone 6 (Fig. 2). In plan view, their strikes are parallel to the salt pillow, i.e., NNE to NE with an average N153 strike (Fig. 2; Table 1). Their length ranges from 1000 to 1800 m, while throws vary from 5 to 40 m. The number of keystone faults is greater at horizons H1 and H5 than near horizons H3 and T7, reaching ~500 and ~390 in the former and ~260 and ~230 in the latter (Fig. 9). Consequently, keystone faults' spacing at horizons H1 and H5 is much smaller than at horizons H3 and T7 (Fig. 9). On seismic profiles, keystone faults form small symmetric grabens above a salt pillow (Figs. 5–6). Fault dips range from 45.8° to 63.3°, for a mean dip of 53.3°. Most keystone faults are restricted to the relatively muddier Lower North Sea Group, though a few propagate into the Middle North Sea Group (Figs. 5–6).

Two NE- and N-striking keystone faults were selected to compile throw-length (T_{max}-L) and throw-depth (T-Z) plots, keystone fault 1 (KF1) and 2 (KF2) (Fig. 2). They are 1280 and 1760 m long, and dip

respectively to the NEE and NW (Fig. 2). Both are isolated faults, as they have rugged curve profiles that show the highest throw near the centre but the lowest throw at the fault tips in T_{max}-L data (Fig. 14a–b). Fault KF1 offsets the strata between horizons H0 and H9, while KF2 offsets strata between horizons H0 and NU (Upper North Sea Group). The upper part of KF1 is bounded by horizons H8 or H9, while the upper part of KF2 is limited by horizon NU. Both faults record throw maxima near horizon H6 (Fig. 14), indicating they probably first nucleated at this horizon. Multiple throw minima are visible on T-Z plots, implying they were formed by the dip linkage of distinct fault segments (Fig. 14).

6. Stress inversion for faults developed around diapir K09

Radial faults around salt diapirs can be useful to understand the orientation of principal palaeostress tensors (e.g. Quintà et al., 2012). Radial faults are ubiquitous around diapir K09 and can be divided into six zones based on their geometry, orientation and distribution (Fig. 2). In parallel, polygonal faults are aligned (Fig. 11h–i), indicating they have been influenced by the superposition of regional and local stresses. As local stresses in the study area were mainly caused by the rise of diapir K09, stress inversions for these polygonal faults provide useful data to understand the stress state around the diapir of interest, though polygonal faults are regarded as non-tectonic faults. Considering polygonal faults occur in two distinct tiers, we inverted palaeostress conditions separately for each tier, i.e. for 4,788 faults in Tier 1 and 1, 571 faults in Tier 2 (Fig. 15; Table 2). Stress inversions were also applied to the 792 keystone faults mapped close to diapir K09 (Fig. 15; Table 2).

The results of our stress inversion show that maximum principal
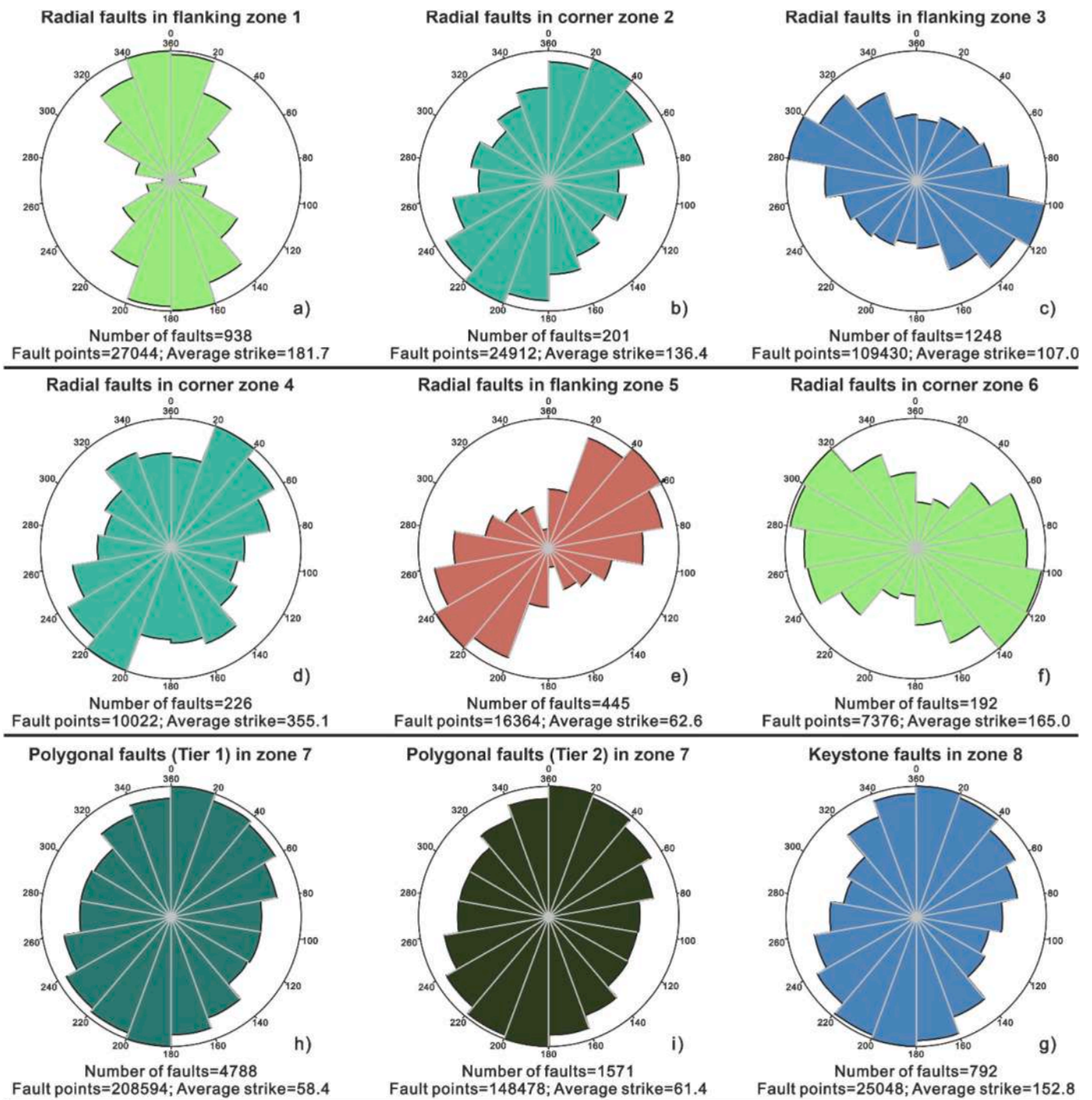
Fig. 11. Rose diagrams showing the strike of faults in each interpreted zone, plotted using fault-point data. a) Radial faults in flanking zone 1. b) Radial faults in corner zone 2. c) Radial faults in flanking zone 3. d) Radial faults in corner zone 4. e) Radial faults in flanking zone 5. f) Radial faults in corner zone 6. g) Polygonal faults (Tier 1) in zone 7; h) Polygonal faults (Tier 2) in zone 7; i) Keystone faults in zone 8.

stress tensors (σ_1) are nearly vertical in all eight zones (Table 2). Accordingly, intermediate (σ_2) and minimum (σ_3) principal stress tensors are nearly horizontal (Table 2). It is important to note that the minimum principal stresses obtained from all flanking and corner zones form a triangular stress ring around diapir K09 (Fig. 15). The width of

this stress ring correlates with the width of flanking or corner zones developed around the diapir, but with marked variations. Also, the width of flanking and corner zones developed around diapir K09 varies with depth (Figs. 9 and 16). For instance, the width of flanking zone 3 is around 2.2 km near horizon 1 (Fig. 9h), but increases to around 4.4 and
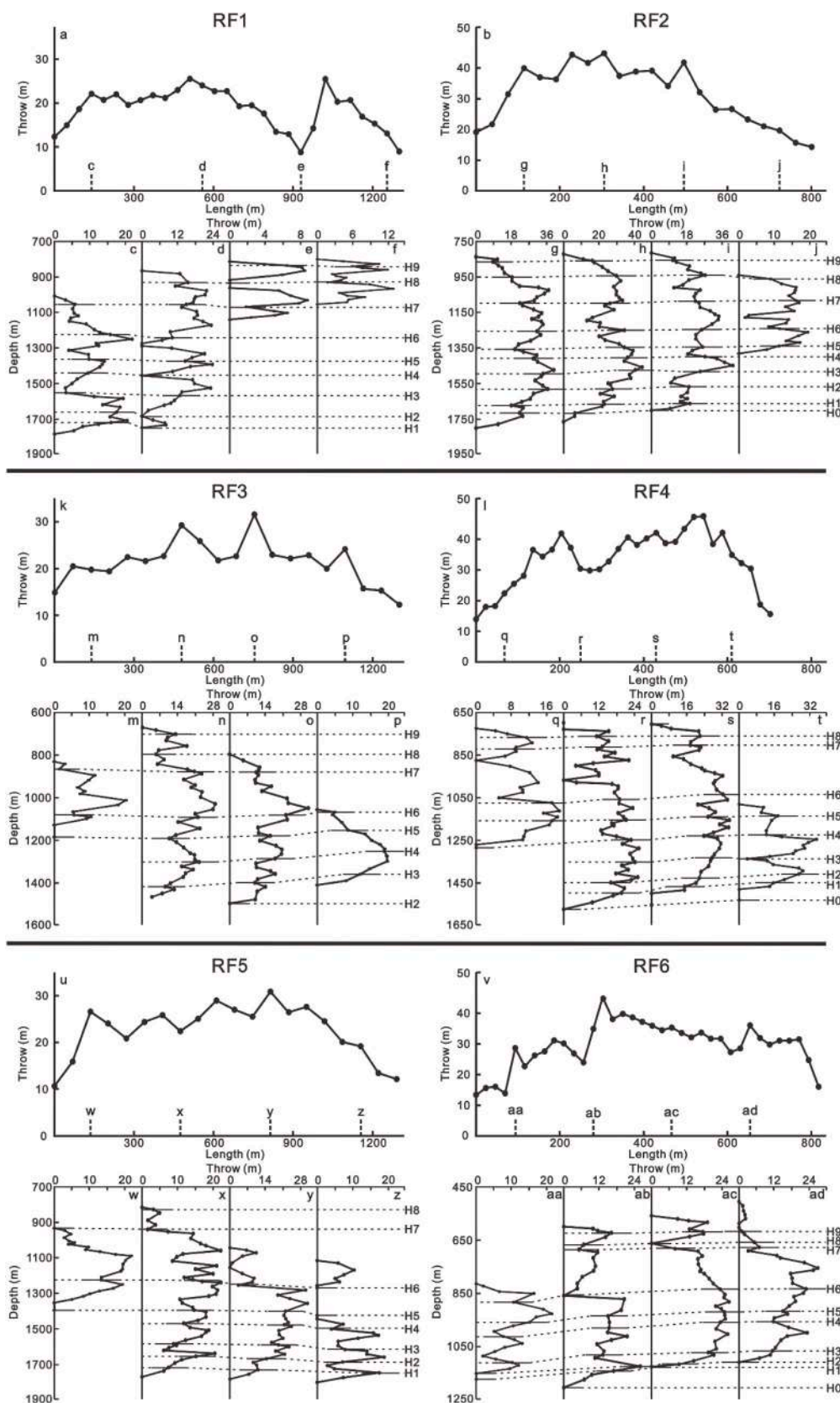
Fig. 12. Throw-length along fault (T_{max}-L) and throw-depth (T–Z) plots for radial fault 1 (RF1) to radial fault 6 (RF6), which are shown in Figs. 2 and 5–7. The vertical dashed lines c-j, m-t and w-ad in the T_{max}-L plots above indicate the location of the T-Z plots just below. Dashed lines mark the seismic-stratigraphic horizons interpreted in this study.
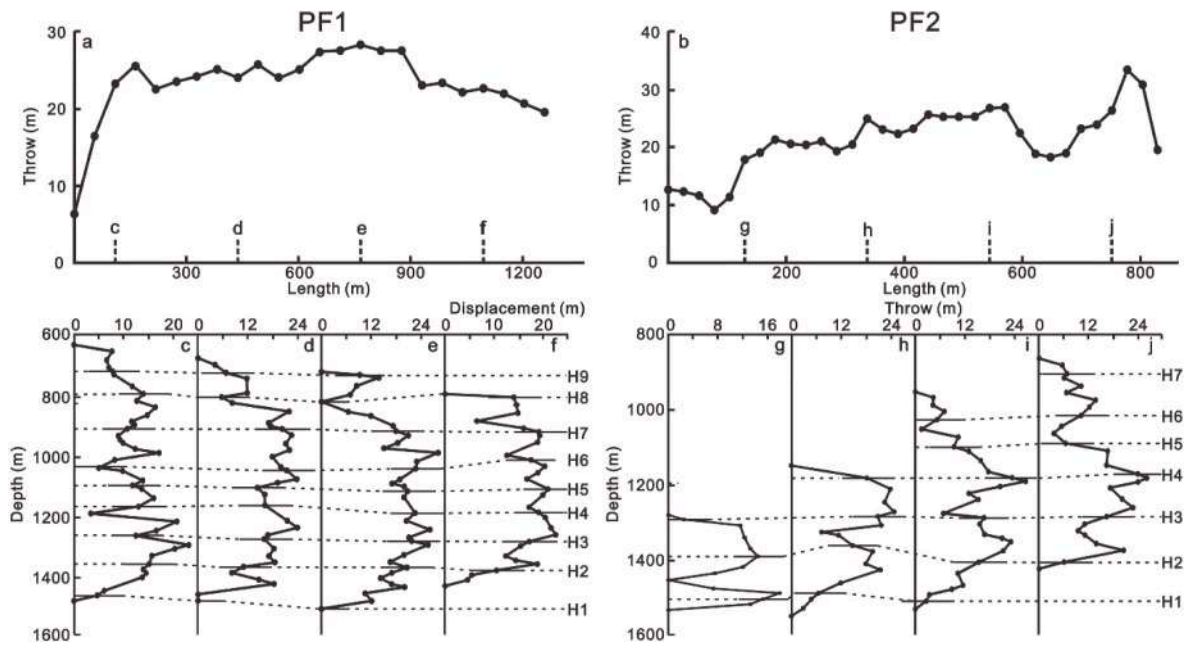
Fig. 13. Throw-length along fault (T_{max}-L) and throw-depth (T–Z) plots for polygonal faults 1 (PF1) and 2 (PF1), which are shown in Figs. 2 and 16. The vertical dashed lines c-j in the T_{max}-L plots above indicate the location of the T-Z plots just below. Dashed lines mark the seismic-stratigraphic horizons interpreted in this study.
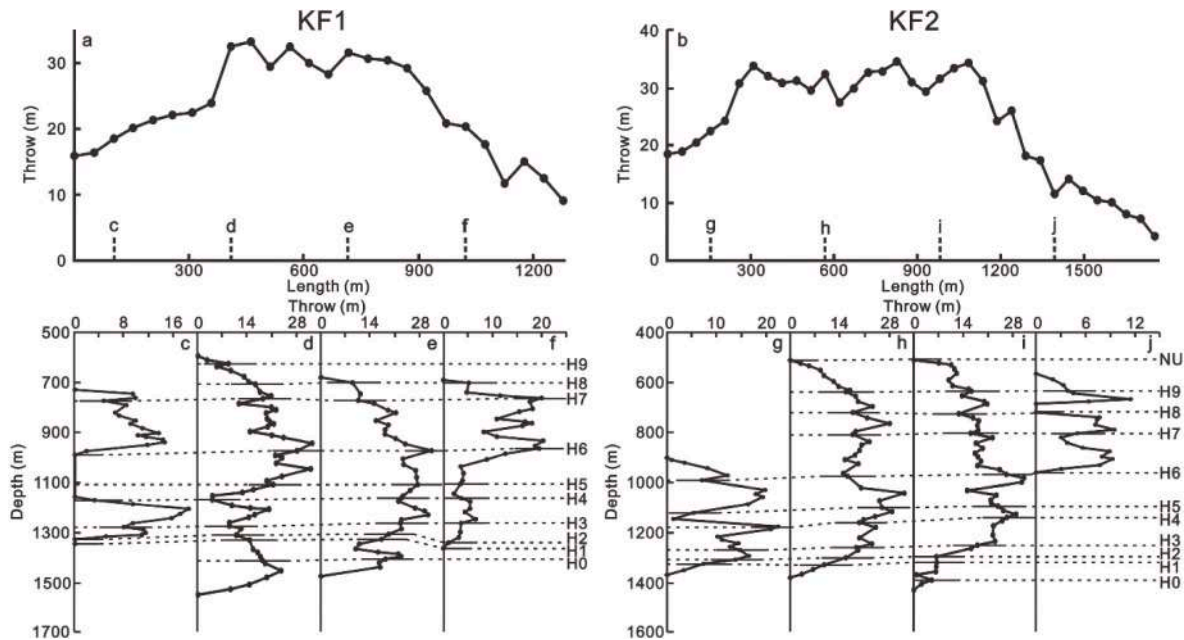

Fig. 14. Throw-length along fault (T_{max}-L) and throw-depth (T–Z) plots for keystone faults 1 (KF1) and 2 (KF2), as shown in Figs. 2 and 5. The vertical dashed lines c-j in the T_{max}-L plots above indicate the location of the T-Z plots just below. Dashed lines mark the seismic-stratigraphic horizons interpreted in this study.

3.3 km at horizons H3, H5 and H7, respectively (Fig. 9f, d and 9b). The width of flanking and corner zones is also different among the six zones (Figs. 9 and 16), a character that is mainly associated with presence of adjacent salt structures. For example, flanking zones 1 and 5 are wider than flanking zone 3 at different depths (Fig. 16). In addition, minimum

principal stresses obtained from radial faults in zones 1, 3 and 5 are parallel to the flanks of diapir K09 (Fig. 15). Conversely, minimum principal stresses obtained from corner zones 2, 4 and 6 are normal to the directions of its corner bisector (Fig. 15). Interestingly, the minimum principal stresses obtained from the two tiers of polygonal faults have
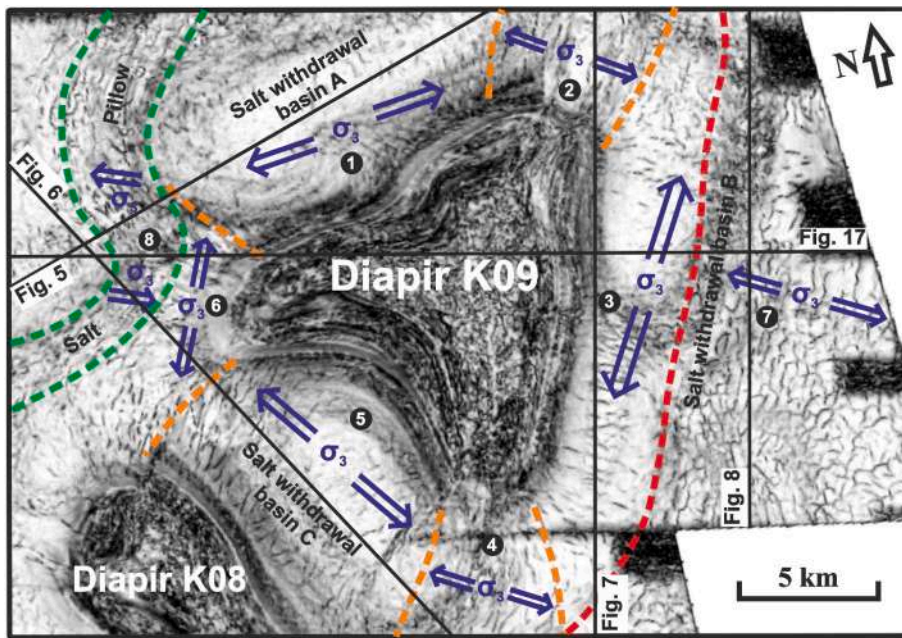
Fig. 15. Variance time-slice (Z=−1100 ms two-way time) showing the minimum principal palaeostress tensors (σ₃) obtained from stress inversions for each zone. The direction of minimum principal palaeo-stress for each zone is highlighted by blue arrows. Six flanking or corner zones are separated by orange dash lines and labelled 1 to 6. Zones where polygonal and keystone faults were developed are bounded by red or green lines, which are labelled 7 and 8, respectively. The seismic profiles in Figs. 5–8 and 17 are shown by black lines.
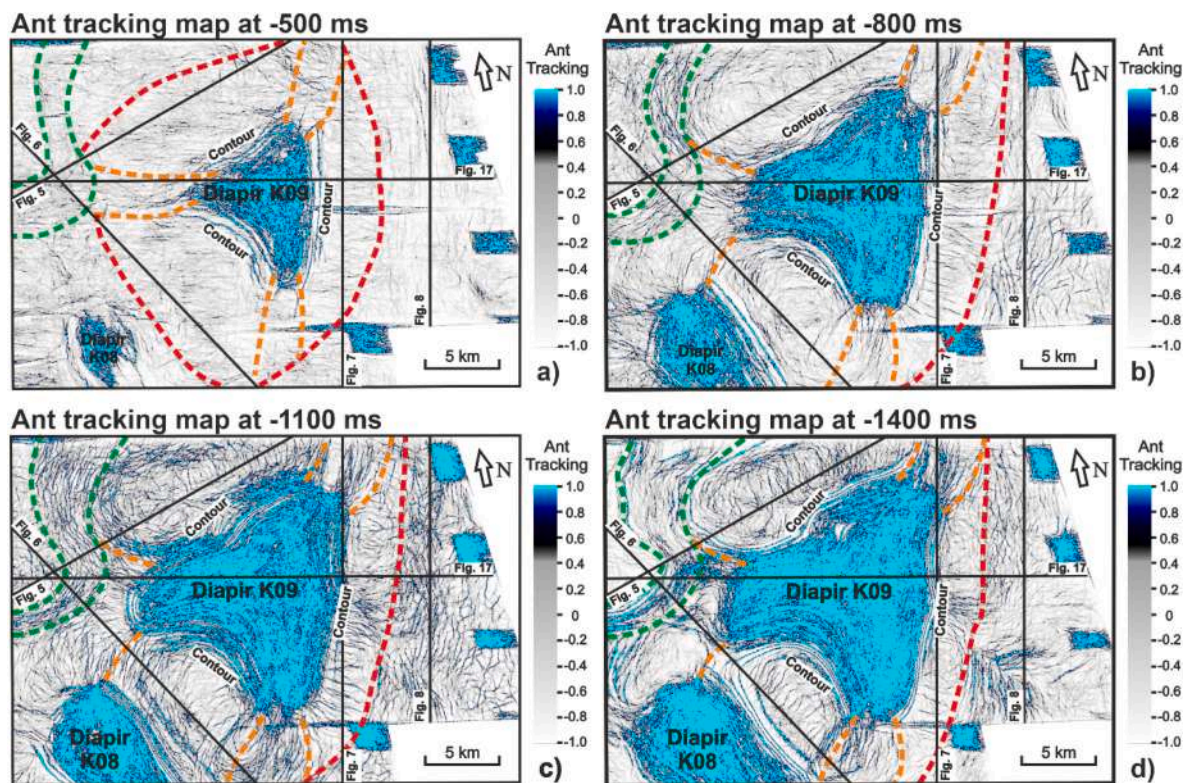

Fig. 16. Ant tracking maps at different depths in the study area showing the width change of flanking and corner zones around salt diapir K09 with depth. Contour lines developed around diapir K09 indicates the areas in which strata are more folded and rarely crossed by faults. Six flanking or corner zones are separated by orange dash lines. The zones where polygonal and keystone faults were developed are bounded by red or green lines. a-d) Ant tracking maps at −500, −800, −1100 and −1400 ms, respectively. The seismic profiles in Figs. 5–8 and 17 are shown by black lines.
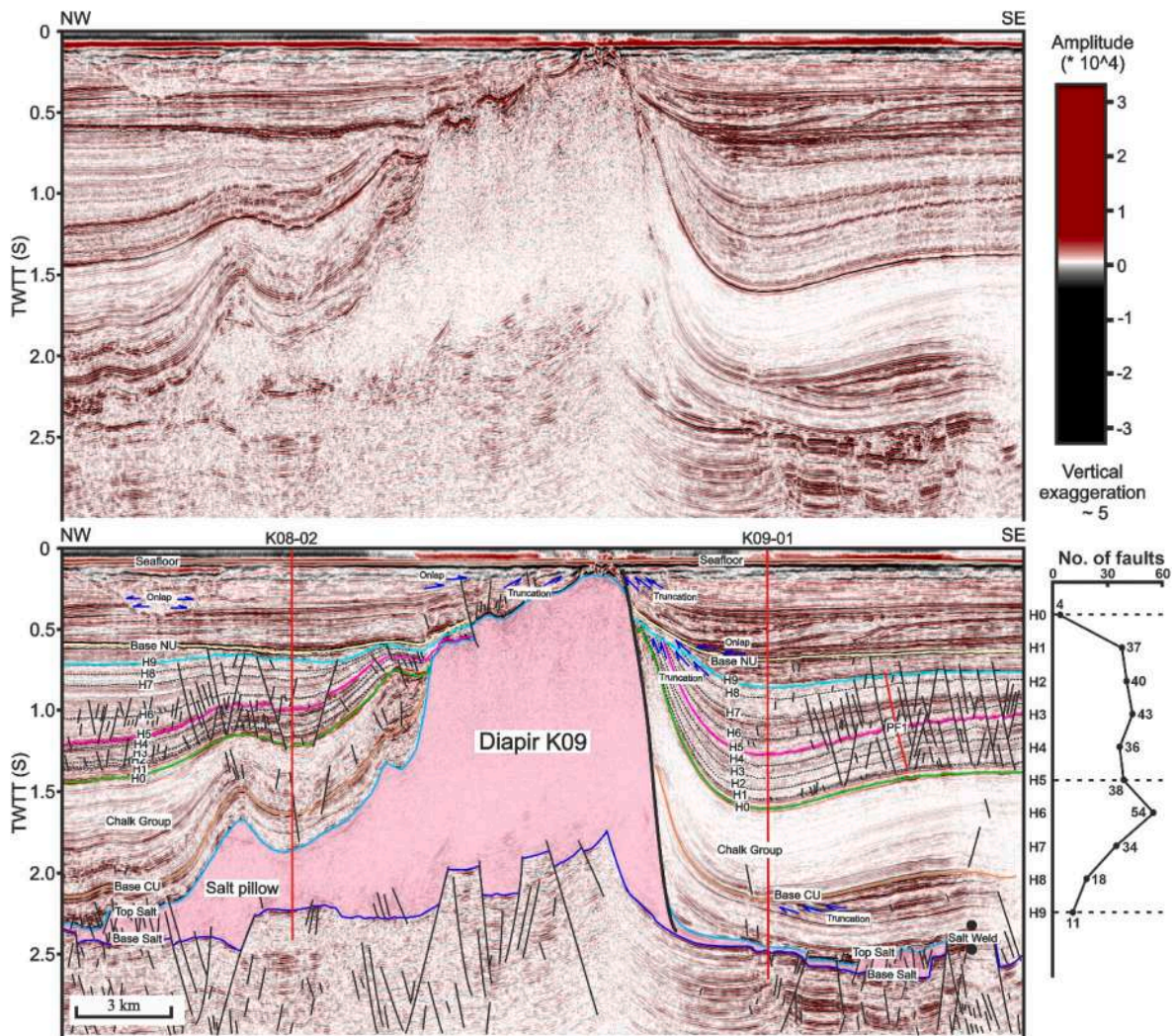
Fig. 17. Seismic profile across salt diapir K09 highlighting the thinning of strata towards it. Eight seismic horizons correlated with wells K08–02 and K09-01 are shown by lines and labels with different colours, whereas seven other horizons are shown by black dash lines and labels. Faults are represented by black or red lines, including polygonal fault 1 (PF1). Wells K08–02 and K09-01 are shown by red bold lines. A salt weld is shown by two black circles. Plot on the right of seismic section shows the number of faults intersecting different horizons on the seismic profile. The location of the seismic profile is shown in Fig. 2. CU-Chalk Group.

similar directions, and they are nearly normal to the boundary between the polygonal and radial faults (Fig. 15). Finally, the minimum principal stresses estimated from keystone faults are near-normal to the strike of their underlying salt pillow (Fig. 15).

7. Discussion

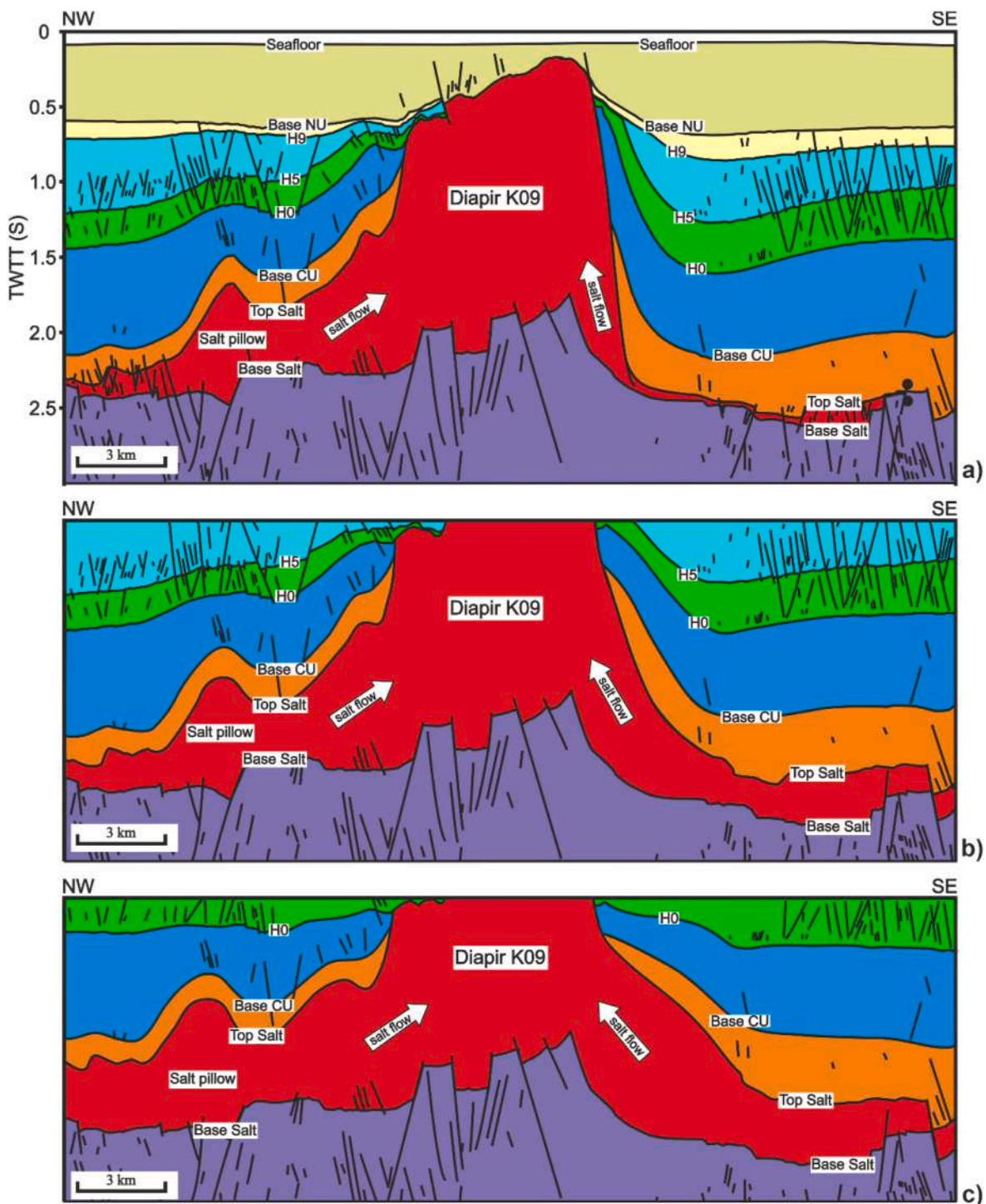### 7.1. Structural evolution of salt structures

As the largest salt structure in the study area, diapir K09 has experienced several phases of growth since the Late Permian. Halokinesis first occurred from Middle Triassic to Early Cretaceous, as indicated by the relative thinning of strata between the top salt and CU horizons towards the flanks of the diapir (Figs. 10 and 17). The precise time for the onset of halokinesis is not clear due to the large depositional hiatus spanning part of the Triassic and the whole of Jurassic strata on the Cleaver Bank High, a character resulting from Mid and Late Kimmerian erosion (Remmelts, 1995). Halokinesis, nonetheless, also occurred during the Late Cretaceous as shown by the thinning of the Chalk Group towards the diapir (Figs. 17 and 18). This halokinesis likely responded to active diapirism driven by Late Cretaceous tectonic inversion (Laramide Inversion; Wong et al., 2007; Fattah et al., 2012; Harding and Huuse,

2015). Overburden loading was probably a secondary process driving halokinesis at this time, and was in great part promoted by the presence of a relatively thick (1300 m) Chalk Group (see well K09-01 in Fig. 4).

Diapir K09 continued its growth in the Paleogene, forming three salt-withdrawal basins around its flanks (Figs. 2, 17 and 18). Significant halokinesis occurred between the Eocene and Oligocene in association with Pyrenean tectonic inversion (Harding and Huuse, 2015). It generated an angular unconformity between the Lower and the Middle North Sea Groups (Horizon H9) (Figs. 17 and 18). It also caused local stress perturbations around diapir K09 during its rise, resulting in the alignment of adjacent polygonal faults (Fig. 11) and the near emersion of diapir K09 at the surface (Fig. 18c).

Important halokinesis also occurred in the Oligocene and Miocene in association with Savian tectonic inversion, as revealed by the angular unconformity separating Paleogene from Neogene strata at the base of the Upper North Sea Group (Fig. 17). At this time, the three salt-withdrawal basins in the study area became shallower, denoting the gradual burial of diapir K09 (Figs. 5, 6, 17 and 18). With increasing deposition, diapir K09 was gradually covered by Neogene strata. It nevertheless continued to grow in the Late Neocene and Quaternary, leading to important thinning of the Upper North Sea Group (Figs. 17–18a).

Fig. 18. Section showing the Cenozoic evolution of salt diapir K09 and surrounding faults in three structural stages. a) Stage 3 (between horizon H9 and the Seafloor) marks a relative quiescence of halokinesis, forming a few radial faults and keystone faults. b) Stage 2 (between horizons H5 and H9) records significant halokinesis, leading to the formation of a great number of radial and keystone faults, whereas polygonal faults are limited to the southeast part of the section. c) Stage 1 (between horizons H0 and H5) is characterised by important halokinesis and increasing numbers of radial faults, while polygonal faults to the southeast part of the section. The location of the section, based on the seismic profile in Fig. 17, is shown in Fig. 2. CU-Chalk Group.

The triangular shape, in plan view, of diapir K09 is attributed to the existence of a large NE-striking Mesozoic fault zone and adjacent salt-withdrawal basins (Fig. 17). This NE-striking fault controlled the morphology of the eastern flank of diapir K09 during the Mesozoic. With the later (Cenozoic) rise of diapir K09 and adjacent salt structures, its north and southwest flanks were formed due to the development of salt-withdrawal basins A and C. This also explains why the east flank of diapir K09 is less curved than its north and southwest flanks (Fig. 16).

As for the salt pillow in the study area, it was formed during Late Cretaceous tectonic inversion (Figs. 17 and 18), as suggested by the fact that the Chalk Group is relatively thin above this pillow. The salt pillow continued growing during the Paleogene, resulting in the further thinning of Lower North Sea Group above it (Figs. 17 and 18).

7.2. A model explaining how halokinesis controlled the formation and development of surrounding fault families

Halokinesis exerts an important control on the fault families surrounding diapir K09, including on their geometries and strikes. In the study area, faults are well developed in Paleogene clay or shale, but their geometry, orientation and spacing show marked differences with depth (Fig. 9). Faults developed around diapir K09 have also experienced multiple evolution stages. In this work we suggest that halokinesis controlled the formation and growth of the interpreted fault families in three distinct stages (Fig. 18).

Stage 1, represented by the interval between horizons H0 and H5, records important halokinesis due to an increase in the vertical loading imposed by the sediment actively filling the salt-withdrawal basins around diapir K09 (Fig. 18c). At the start of Stage 1, between horizons H0 and H2, halokinesis was moderate as limited Paleogene strata were deposited around diapir K09. Polygonal faulting predominated at this time, covering a large area of salt-withdrawal basin B and parts of salt-withdrawal basins A and C (Fig. 9g–h). These polygonal faults were randomly distributed in terms of their locations and strikes at this stage, but closely spaced and with small throws. Radial faults were limited to a small area near diapir K09, particularly within salt-withdrawal basin B (Fig. 9g–h). This basin was at this time only bounded by diapir K09, a character resulting in limited stretching during the rise of this salt structure (Figs. 2 and 9). Comparatively, salt–withdrawal basins A and C were also bounded by other salt structures; stretching associated with the rise of diapir K09 and adjacent salt structures affected a relatively large area in these two basins (Figs. 2 and 9).

Halokinesis was intensified between horizons H2 and H5 due to the deposition of increasingly larger volumes of sediment around diapir K09. Thinning of strata is observed towards diapir K09 between the two latter horizons (Fig. 17). Radial faults spanned a relatively wide area at this time as stretching imposed by the rise of diapir K09 was also intensified (Fig. 9c–f). Some of these radial faults started to link with polygonal faults, as suggested by their T-Z plots, proving that radial faults were formed by the dip linkage of discrete segments (Fig. 12). Comparatively, polygonal faults were limited to the eastern part of basin B (Fig. 9e–f). In addition, the length and spacing of polygonal faults were enhanced near horizon H5 (Fig. 9e–f), where polygonal planforms are clearly observed (Fig. 9c–d). Polygonal faults in Tier 1 were aligned to the NE (Figs. 9e,f and 11h), a direction related to NW-SE stretching caused by underlying salt withdrawal towards diapir K09 (Fig. 18).

Stage 2, represented by strata and structures between horizons H5 and H9, records significant halokinesis – likely due to the combined effect of Pyrenean tectonic inversion and sediment loading (Harding and Huuse, 2015) (Fig. 18b). Radial faults were developed in a relatively small area, and their number sharply decreased at this stage, likely due to the rapid rise of diapir K09. This facilitated the folding of clayey and shaley strata adjacent to this structure, but inhibited the development of radial faults (Figs. 17 and 18) (e.g. Alsop et al., 2000). Moreover, the increase in overburden loading around diapir K09 resulted in a slight decrease in the width of the flanking and corner zones, as overburden loading controlled the lateral limit of hoop stresses (Carruthers et al., 2013). Hence, fewer radial faults were developed during Stage 2 when compared to Stage 1, while radial faults were developed in a smaller area. Radial faults were also linked to other faults in greater numbers, forming large linked structures during Stage 2 (Fig. 7). These large radial faults offset horizons H0 to H9, with throw minima occurring near horizon H9 (Fig. 12). These throw minima suggest their upper tips are truncated by horizon 9, the regional unconformity associated with the Pyrenean inversion episode.

Similarly to Stage 1, polygonal faults were developed in the eastern part of basin B and their number is higher at horizon H7 compared to horizons H3 and H5 (Fig. 9a–b). This is because many polygonal faults in Tier 2 cross-cut horizon H7. Additionally, several polygonal faults were dip-linked with other polygonal faults, as shown by their T-Z plots

(Fig. 13). During Stage 2, Polygonal faults in Tier 2 were also aligned to the NE due to halokinesis. Finally, keystone faults were developed above the salt pillow during this stage, accompanying Pyrenean tectonic inversion, and agreeing with the observation that most keystone faults are bounded by horizon H9. Keystone faults were also linked to other faults during Stage 2, as shown in T-Z data (Fig. 14).

Stage 3, comprising strata between horizon H9 and the seafloor, is characterised by a relative quiescence of halokinesis (Fig. 18a), as there was no major influence of tectonic inversion on the study area (Harding and Huuse, 2015). Although Savian tectonic inversion occurred at this stage, it had a minor influence when compared to the Pyrenean inversion (De Jager, 2003; De Lugt et al., 2003; De Lugt, 2007). Locally, sedimentation rates exceeded the rate of salt rise, resulting in the blanketing of diapir K09 by strata (Fig. 17). As a result, faults were mainly developed below horizon NU, the unconformity separating Paleogene and Neogene strata. Very few radial faults were formed around diapir K09, as halokinesis was minor, while polygonal faults stopped forming as relatively coarse sandy clay, silty sandstone and sandstone were deposited between horizon H9 and the seafloor. A few large keystone faults were developed by dip linkage during Savian tectonic inversion (Fig. 14), but their number is markedly lower than in Stage 2. Their upper tips were truncated by horizon NU, accompanying the abrupt throw minima observed in Fig. 14.

7.3. Stress state around triangular salt diapirs

Diapir K09 developed as a rising triangular salt structure and was affected by two Cenozoic episodes of tectonic inversion. This led to the formation and development of multiple faults under a complex stress field. Stress inversions for the interpreted faults show that maximum principal palaeostresses (σ_1) were nearly vertical in all eight zones, whereas intermediate (σ_2) and least principal palaeostresses (σ_3) were sub-horizontal (Fig. 15; Table 2). This indicates that maximum principal stresses in all eight zones resulted from overburden loading. In addition, the combination of all minimum principal stresses obtained from radial faults show a triangular stress ring around diapir K09 (Fig. 15), implying that minimum principal stresses in all flanking and corner zones derived from local stretching related to the rise of this diapir. Against this backdrop, strain in flanking zones show marked differences when compared with corner zones. Strain in the flanking zones spans a much larger area than in the corner zones (Fig. 15). The number of radial faults developed in flanking zones is also greater than in corner zones of diapir K09 (Table 1), proving that greater stretching occurred in the former (flanking) zones. Minimum principal stresses in flanking zones are naturally parallel to the flank of diapir K09, whereas in corner zones are normal to the direction of the corner bisector (Fig. 15). The corner radial faults are thus formed in a transition zone between two contiguous flanking zones. In addition, strata folding is more likely to be observed in flanking zones compared with corner zones, as shown by the distinct contour lines developed around diapir K09 (Fig. 16). These contour lines highlight the areas in which strata are more folded and rarely crossed by faults (Figs. 16, 17 and 19). Furthermore, flanking radial faults are usually deeper than corner radial faults (Fig. 9), and they are also steeper than the latter (Fig. 19), a character implying that there are significant differences in vertical loading and compaction between flanking and corner zones, influencing local stress fields. Hence, the stress field around a triangular salt diapir is complex and markedly distinct from the relative homogeneous stress field of a circular salt diapir.

The width of the perturbed stress field around diapir K09 varied at different stages, leading to changes in the width of flanking and corner zones (Figs. 9 and 16). As the salt movement intensified, the width of flanking and corner zones increased (Figs. 9 and 16), indicating that the triangle-shaped stress rim also increased around the diapir. However, overburden loading could also impose an important influence on the width of the stress field around diapir K09. With the increasing loading
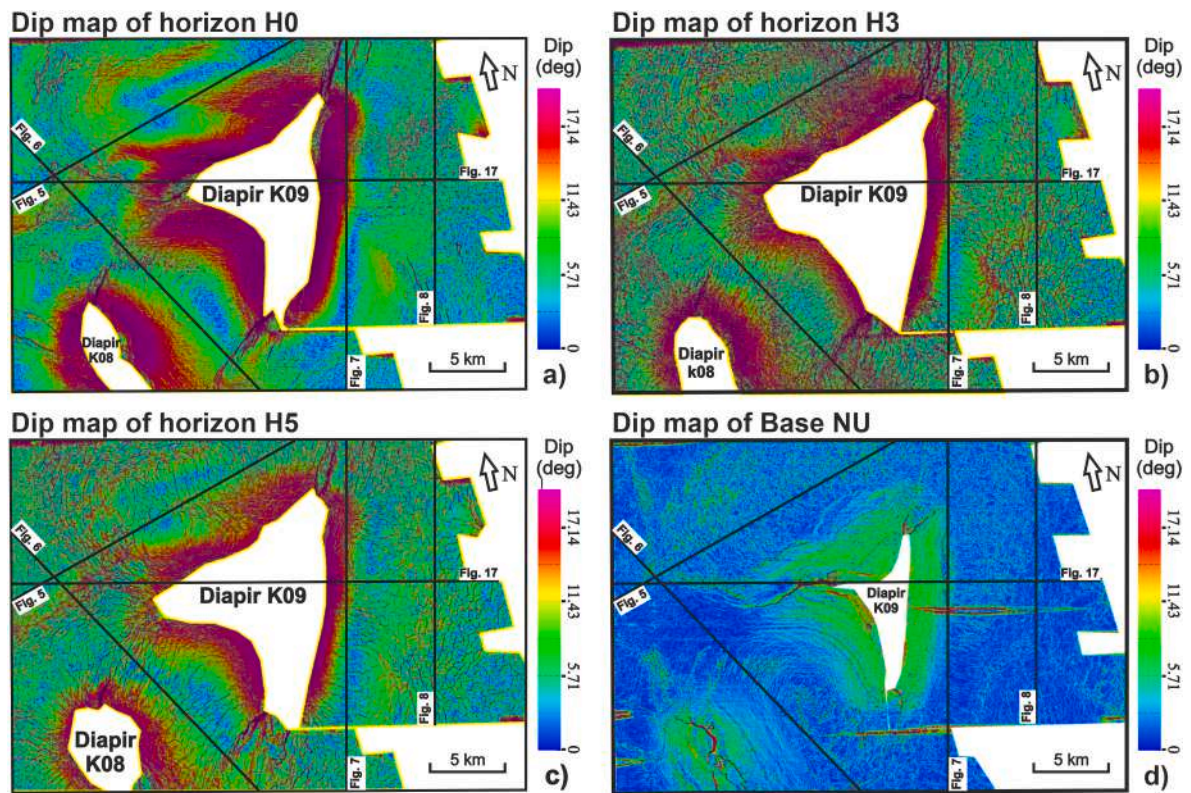
Fig. 19. Dip maps of key horizons in the study area highlighting the fact that dips in flanking zones are much larger than in corner zones at different horizons. a-d) Dip maps of horizons H0, H3, H5 and Base NU, respectively. The seismic profiles shown in Figs. 5–8 and 17 are shown by black lines. NU-Upper North Sea Group.

from overburden strata, a slight decrease in the width of this stress field is observed around this diapir (Fig. 9b–d), a character agreeing with the mechanism proposed by Carruthers et al. (2013) in which radial loading of overburden around a circular salt diapir controls the lateral limit of hoop stresses. However, in contrast to Carruthers et al. (2013), salt structures developed near diapir K09 have also largely influenced the stress field around this latter structure, though their importance was dependent on their position, distance and strike. For example, flanking zones 1 and 5 spanned a much broader area than zone 3 (Fig. 9), showing that the overlapping hoop stresses produced by nearby salt structures and diapir K09, along similar strikes, increased the width of the stretching stress field in flanking radial zones 1 and 5. Comparatively, the stress field above the salt pillow was rarely influenced by diapir K09 as the minimum principal stress was nearly normal to the strike of the pillow (Fig. 15). The development of this salt pillow nevertheless limited the width of the extensional stress field produced by diapir K09 (Fig. 15).

Polygonal faults are mainly aligned in a NE-SW direction (Figs. 9, 11h and 11i), indicating they were influenced by local stresses. In the Paleogene, regional tectonic stresses in the study area were dominated by NW-SE compression (Ligtenberg et al., 2011; Van Ojik et al., 2020), which had a limited influence on fault strikes. However, minimum principal stresses estimated for the two polygonal fault tiers are also NW-SE striking, a direction normal to the boundary between the polygonal faults and flanking zone 3 (Fig. 15). This suggests that the strike of polygonal faults was controlled by the movement of underlying salt towards diapir K09 (Fig. 18). Therefore, the rise of diapir K09 indirectly influenced the stress field in the outer part of flanking zone 3, resulting in the preferred arrangement of polygonal faults in a NE-SW direction.

8. Conclusions

This work aimed at understanding the palaeostress state around a rising triangular salt diapir, information with key implications to carbon sequestration, gas storage and the production of subsurface oil and gas around salt diapirs. Faults developed around diapir K09, located on the Cleaver Bank High, Southern North Sea, were analysed in detail, and stress inversions were completed to reveal the palaeostress state around this salt structure. The main conclusions of this work can be summarised as follows:

a) Structures around diapir K09 include radial, polygonal and keystone faults, which are separated into eight distinct zones based on their geometry, strike and overall distribution. Radial faults were developed in flanking or corner zones as a way to accommodate stretching during the rise of diapir K09. Polygonal faults were preferentially aligned in the outer part of flanking zones. Keystone faults were mainly controlled by the rise of a salt pillow during Paleogene tectonic inversion.

b) Diapir K09 has experienced multiple phases of growth, with two of these being associated with Cenozoic tectonic inversion. Three salt-withdrawal basins were formed along the flanks of diapir K09. A salt pillow was developed during Late Cretaceous tectonic inversion and was amplified during Pyrenean and Savian tectonic inversion.

c) Halokinesis controlled the generation and growth of fault families in three structural stages. Stage 1 recorded the gradual intensification of halokinesis, resulting in an increase in the number of radial faults, while polygonal faults were limited to a small area. Stage 2 was characterised by significant halokinesis, leading to the formation of a great number of radial faults and keystone faults, whereas polygonal faults remained limited to a small area. Stage 3 is marked by moderate halokinesis, forming a few radial faults and keystone faults.

d) Stress inversions for structures interpreted in each zone reveal that maximum principal palaeostress is nearly vertical, whereas intermediate and minimum principal palaeostress are sub-horizontal. Palaeostresses in flanking zones are different from corner zones. The combination of minimum principal palaeostresses from all flanking and corner zones forms a triangle-shaped hoop stress ring around diapir K09.

In summary, the width of the latter stress ring was not only associated with the growth of salt diapir, but also strongly influenced by adjacent salt structures. Minimum principal palaeostresses obtained from two tiers of polygonal faults were nearly normal to the boundary between the polygonal and radial faults due to local extension caused by halokinesis. Comparatively, the minimum principal palaeostress in the zone where keystone faults were developed is nearly normal to the strike of the salt pillow below, indicating they were nearly free of any stress perturbations caused by the rise of diapir K09.

Declaration of competing interest

Data availability

The data that has been used is confidential.

Acknowledgements

Appendix A. Supplementary data

Supplementary data to this article can be found online at https://doi.org/10.1016/j.marpetgeo.2023.106385.

References

Alberts, M.A., Underhill, J.R., Spencer, A., 1991. The Effect of Tertiary Structuration on Permian Gas Prospectivity, Cleaver Bank Area, Southern North Sea, UK: Generation, Accumulation, and Production of Europe's Hydrocarbons, vol. 1. European Association of Petroleum Geoscientists Special Publication, pp. 161–173. https://doi.org/10.1016/j.tecto.2014.07.015.

Alsop, G.I., 1996. Physical modelling of fold and fracture geometries associated with salt diapirism. Geological Society, London, Special Publications 100 (1), 227–241. https://doi.org/10.1144/gsl.sp.1996.100.01.14.

Alsop, G., Brown, J., Davison, I., Gibling, M., 2000. The geometry of drag zones adjacent to salt diapirs. J. Geol. Soc. 157 (5), 1019–1029. https://doi.org/10.1144/jgs.157.5.1019.

Alves, T.M., 2012. Scale-relationships and geometry of normal faults reactivated during gravitational gliding of Albian rafts (Espirito Santo Basin, SE Brazil). Earth Planet Sci. Lett. 331, 80–96. https://doi.org/10.1016/j.epsl.2012.03.014.

Angelier, J., 1990. Inversion of field data in fault tectonics to obtain the regional stress—III. A new rapid direct inversion method by analytical means. Geophys. J. Int. 103 (2), 363–376. https://doi.org/10.1111/j.1365-246X.1990.tb01777.x.

Behlau, J., Mingerzahn, G., 2001. Geological and tectonic investigations in the former Morsleben salt mine (Germany) as a basis for the safety assessment of a radioactive waste repository. Eng. Geol. 61 (2–3), 83–97. https://doi.org/10.1016/s0013-7952(01)00038-2.

Bradley, W. B., Bore hole failure near salt domes, *in* Proceedings SPE Annual Fall Technical Conference and Exhibition 1978, OnePetro. https://doi.org/10.2118/7503-ms.

Brown, A.R., 2011. Interpretation of Three-Dimensional Seismic Data. Society of Exploration Geophysicists and American Association of Petroleum Geology. https://doi.org/10.1306/M4271346.

Carruthers, D., Cartwright, J., Jackson, M.P., Schutjens, P., 2013. Origin and timing of layer-bound radial faulting around North Sea salt stocks: new insights into the evolving stress state around rising diapirs. Mar. Petrol. Geol. 48, 130–148. https://doi.org/10.1016/j.marpetgeo.2013.08.001.

Cartwright, J.A., 1994. Episodic basin-Wide hydrofracturing of overpressured early cenozoic mudrock sequences in the North Sea basin. Mar. Petrol. Geol. 11 (5), 587–607. https://doi.org/10.1016/0264-8172(94)90070-1.

Cartwright, J., 2011. Diagenetically induced shear failure of fine-grained sediments and the development of polygonal fault systems. Mar. Petrol. Geol. 28 (9), 1593–1610. https://doi.org/10.1016/j.marpetgeo.2011.06.004.

Cartwright, J., Lonergan, L., 1996. Volumetric contraction during the compaction of mudrocks: a mechanism for the development of regional-scale polygonal fault systems. Basin Res. 8 (2), 183–193. https://doi.org/10.1046/j.1365-2117.1996.01536.x.

Cartwright, J., James, D., Bolton, A., 2003. The genesis of polygonal fault systems: a review. Geological Society, London, Special Publications 216 (1), 223–243. https://doi.org/10.1144/gsl.sp.2003.216.01.15.

Chang, K.W., Hesse, M.A., Nicot, J.-P., Hovorka, S.D., 2011. Effects of adjacent mud rocks on CO2 injection pressure: model case based on a typical US Gulf Coast salt diapir field under injection. Energy Proc. 4, 4567–4574. https://doi.org/10.1016/j.egypro.2011.02.415.

Chen, P., 2016. Fault Reactivation Analysis of the Cleaver Bank High Based on 3D Seismic Data.

Chiaramonte, L., Zoback, M.D., Friedmann, J., Stamp, V., 2008. Seal integrity and feasibility of CO 2 sequestration in the Teapot Dome EOR pilot: geomechanical site characterization. Environ. Geol. 54, 1667–1675. https://doi.org/10.1007/s00254-007-0948-7.

Coleman, A.J., Jackson, C.A.-L., Duffy, O.B., Nikolinakou, M.A., 2018. How, where, and when do radial faults grow near salt diapirs? Geology 46 (7), 655–658. https://doi.org/10.1130/g40338.1.

Cowie, P.A., Scholz, C.H., 1992. Displacement-length scaling relationship for faults: data synthesis and discussion. J. Struct. Geol. 14 (10), 1149–1156. https://doi.org/10.1016/0191-8141(92)90066-6.

Cox, S., Knackstedt, M., Braun, J., 2001. Principles of Structural Control on Permeability and Fluid Flow in Hydrothermal Systems. https://doi.org/10.5382/rev.14.01.

Davison, I., Bosence, D., Alsop, G.I., Al-Aawah, M.H., 1996. Deformation and sedimentation around active Miocene salt diapirs on the Tihama Plain, northwest Yemen. Geological Society, London, Special Publications 100 (1), 23–39. https://doi.org/10.1144/gsl.sp.1996.100.01.03.

Davison, I., Alsop, G., Evans, N., Safaricz, M., 2000a. Overburden deformation patterns and mechanisms of salt diapir penetration in the Central Graben. North Sea: Mar. Petrol. Geol. 17 (5), 601–618. https://doi.org/10.1016/s0264-8172(00)00011-8.

Davison, I., Alsop, I., Birch, P., Elders, C., Evans, N., Nicholson, H., Rorison, P., Wade, D., Woodward, J., Young, M., 2000b. Geometry and late-stage structural evolution of Central Graben salt diapirs. North Sea: Mar. Petrol. Geol. 17 (4), 499–522. https://doi.org/10.1016/s0264-8172(99)00068-9.

De Jager, J., 2003. Inverted basins in The Netherlands, similarities and differences. Neth. J. Geosci. 82 (4), 339–349. https://doi.org/10.1017/S0016774600020175.

De Lugt, I.R., 2007. Stratigraphical and Structural Setting of the Palaeogene Siliciclastic Sediments in the Dutch Part of the North Sea Basin. UU Dept. of Earth Sciences.

De Lugt, I., Van Wees, J., Wong, T.E., 2003. The tectonic evolution of the southern Dutch North Sea during the Palaeogene: basin inversion in distinct pulses. Tectonophysics 373 (1–4), 141–159. https://doi.org/10.1016/S0040-1951(03)00284-1.

Deckers, J., Rombaut, B., Broothaers, M., Dirix, K., Debacker, T., 2022. New 3D fault model for eastern Flanders (Belgium) providing insights on the major deformation phases in the region since the late Paleozoic. J. Struct. Geol. 104779 https://doi.org/10.1016/j.jsg.2022.104779.

Doornenbal, H., Stevenson, A., 2010. Petroleum Geological Atlas of the Southern Permian Basin Area. EAGE.

Dusseault, M.B., Maury, V., Sanfilippo, F., Santarelli, F.J., 2004. Drilling around salt: risks, stresses, and uncertainties. In: Proceedings Gulf Rocks. OnePetro the 6th North America Rock Mechanics Symposium (NARMS)2004.

Fattah, R.A., Verweij, J., Witmans, N., Ten Veen, J., 2012. Reconstruction of burial history, temperature, source rock maturity and hydrocarbon generation in the northwestern Dutch offshore. Neth. J. Geosci. 91 (4), 535–554. https://doi.org/10.1017/s0016774600000378.

Ferrill, D.A., Morris, A.P., 2008. Fault zone deformation controlled by carbonate mechanical stratigraphy. Balcones fault system, Texas: AAPG Bull. 92 (3), 359–380. https://doi.org/10.1306/10290707066.

Ferrill, D.A., Morris, A.P., McGinnis, R.N., Smart, K.J., Wigginton, S.S., Hill, N.J., 2017. Mechanical stratigraphy and normal faulting. J. Struct. Geol. 94, 275–302. https://doi.org/10.1016/j.jsg.2016.11.010.

Gartrell, A., Zhang, Y., Lisk, M., Dewhurst, D., 2004. Fault intersections as critical hydrocarbon leakage zones: integrated field study and numerical modelling of an example from the Timor Sea, Australia. Mar. Petrol. Geol. 21 (9), 1165–1179. https://doi.org/10.1016/j.marpetgeo.2004.08.001.

Gasanzade, F., Pfeiffer, W.T., Witte, F., Tuschy, I., Bauer, S., 2021. Subsurface renewable energy storage capacity for hydrogen, methane and compressed air–A performance assessment study from the North German Basin. Renew. Sustain. Energy Rev. 149, 111422 https://doi.org/10.1016/j.rser.2021.111422.

Glennie, K., 1997. History of exploration in the southern North sea. Geological Society, London, Special Publications 123 (1), 5–16. https://doi.org/10.1144/gsl.sp.1997.123.01.02.

Harding, R., Huuse, M., 2015. Salt on the move: multi stage evolution of salt diapirs in The Netherlands North Sea. Mar. Petrol. Geol. 61, 39–55. https://doi.org/10.1016/j.marpetgeo.2014.12.003.

Harding, T.P., Lowell, J.D., 1979. Structural styles, their plate-tectonic habitats, and hydrocarbon traps in petroleum provinces. AAPG Bull. 63 (7), 1016–1058. https://doi.org/10.1306/2f9184b4-16ce-11d7-8645000102c1865d.

Hernandez, K., Mitchell, N.C., Huuse, M., 2018. Deriving relationships between diapir spacing and salt-layer thickness in the Southern North Sea. Geological Society, London, Special Publications 469 (1), 119–137. https://doi.org/10.1144/sp469.16.

Hooghvorst, J.J., Harrold, T.W., Nikolinakou, M.A., Fernandez, O., Marcuello, A., 2020. Comparison of stresses in 3D v. 2D geomechanical modelling of salt structures in the Tarfaya Basin. West African coast: Petrol. Geosci. 26 (1), 36–49. https://doi.org/10.1144/petgeo2018-095.

Jackson, M.P., Hudec, M.R., 2017. Salt Tectonics: Principles and Practice. Cambridge University Press. https://doi.org/10.1017/9781139003988.

Jackson, M.P., Talbot, C.J., 1986. External shapes, strain rates, and dynamics of salt structures. Geol. Soc. Am. Bull. 97 (3), 305–323. https://doi.org/10.1130/0016-7606(1986)97%3C305:essrad%3E2.0.co.

Jackson, M.P.A., Vendeville, B.C., Schultzela, D.D., 1994. Structural dynamics of salt systems. Annu. Rev. Earth Planet Sci. 22, 93–117. https://doi.org/10.1146/annurev.ea.22.050194.000521.

Kim, Y.S., Sanderson, D.J., 2005. The relationship between displacement and length of faults: a review. Earth Sci. Rev. 68 (3–4), 317–334. https://doi.org/10.1016/j.earscirev.2004.06.003.

Langer, M., Heusermann, S., 2001. Geomechanical stability and integrity of waste disposal mines in salt structures. Eng. Geol. 61 (2–3), 155–161. https://doi.org/10.1016/s0013-7952(01)00049-7.

Ligtenberg, H., Okkerman, J., De Keijzer, M., 2011. Fractures in the Dutch Rotliegend—An Overview. https://doi.org/10.2110/pec.11.98.0229.

Luo, G., Nikolinakou, M.A., Flemings, P.B., Hudec, M.R., 2012. Geomechanical modeling of stresses adjacent to salt bodies: Part 1—uncoupled modelsStress Around Salt Bodies. AAPG Bull. 96 (1), 43–64. https://doi.org/10.1306/04111110144.

Maia da Costa, A., M da Costa, V., P D Udebhulu, O., Cabral Azevedo, R., Ff Ebecken, N., Co Miranda, A., M de Eston, S., de Tomi, G R Meneghini, J., Nishimoto, K., 2019. Potential of storing gas with high CO2 content in salt caverns built in ultra-deep water in Brazil: greenhouse Gases. Sci. Technol. 9 (1), 79–94. https://doi.org/10.1002/ghg.1834.

Mandl, G., 1999. Faulting in Brittle Rocks: an Introduction to the Mechanics of Tectonic Faults. Springer, Berlin.

Nikolinakou, M.A., Luo, G., Hudec, M.R., Flemings, P.B., 2012. Geomechanical modeling of stresses adjacent to salt bodies: Part 2—poroelastoplasticity and coupled overpressures. AAPG Bull. 96 (1), 65–85. https://doi.org/10.1306/04111110143.

Nikolinakou, M.A., Flemings, P.B., Hudec, M.R., 2014. Modeling stress evolution around a rising salt diapir. Mar. Petrol. Geol. 51, 230–238. https://doi.org/10.1016/j.marpetgeo.2013.11.021.

Omosanya, K.O., 2020. Cenozoic tectonic inversion in the naglfar dome. Norwegian North Sea: Mar. Petrol. Geol. 118, 104461 https://doi.org/10.1016/j.marpetgeo.2020.104461.

Omosanya, K.O., Johansen, S.E., Harishidayat, D., 2015. Evolution and character of supra-salt faults in the easternmost hammerfest basin, SW barents sea. Mar. Petrol. Geol. 66, 1013–1028. https://doi.org/10.1016/j.marpetgeo.2015.08.010.

Ouellet, A., Bérard, T., Desroches, J., Frykman, P., Welsh, P., Minton, J., Pamukcu, Y., Hurter, S., Schmidt-Hattenberger, C., 2011. Reservoir Geomechanics for Assessing Containment in CO2 Storage: a Case Study at Ketzin, vol. 4. Energy Procedia, Germany, pp. 3298–3305. https://doi.org/10.1016/j.egypro.2011.02.250.

Ozarslan, A., 2012. Large-scale hydrogen energy storage in salt caverns. Int. J. Hydrogen Energy 37 (19), 14265–14277. https://doi.org/10.1016/j.ijhydene.2012.07.111.

Peryt, T.M., Halas, S., Petrivna Hryniv, S., 2010. Sulphur and oxygen isotope signatures of late Permian Zechstein anhydrites, West Poland: seawater evolution and diagenetic constraints. Geol. Q. 54, 387–400.

Pollard, D., Saltzer, S., Rubin, A.M., 1993. Stress inversion methods: are they based on faulty assumptions? J. Struct. Geol. 15 (8), 1045–1054. https://doi.org/10.1016/0191-8141(93)90176-B.

Quintà, A., Tavani, S., Roca, E., 2012. Fracture pattern analysis as a tool for constraining the interaction between regional and diapir-related stress fields: poza de la Sal Diapir (Basque Pyrenees, Spain). Geological Society, London, Special Publications 363 (1), 521–532. https://doi.org/10.1144/sp363.25.

Rafavich, F., Kendall, C.S.C., Todd, T., 1984. The relationship between acoustic properties and the petrographic character of carbonate rocks. Geophysics 49 (10), 1622–1636.

Remmelts, G., 1995. In: Fault-related Salt Tectonics in the Southern North Sea. the Netherlands. https://doi.org/10.1306/m65604c12.

Rowan, M.G., Jackson, M.P.A., Trudgill, B.D., 1999. Salt-related fault families and fault welds in the northern Gulf of Mexico. AAPG Bulletin-American Association of Petroleum Geologists 83 (9), 1454–1484. https://doi.org/10.23867/ri0268d.

Quirk, D., 1993. Interpreting the Upper Carboniferous of the Dutch Cleaver Bank High. In: Proceedings Geological Society, London, Petroleum Geology Conference Series 1993, vol. 4. The Geological Society of London, pp. 697–706. https://doi.org/10.1144/0040697.

Sanz, P., and Dasari, G., Controls on in-situ stresses around salt bodies, *in* Proceedings 44th US Rock Mechanics Symposium and 5th US-Canada Rock Mechanics Symposium 2010, OnePetro.

Seymour, K., Rae, G., Peden, J., and Ormston, K., Drilling close to salt diapirs in the North Sea, *in* Proceedings SPE Offshore Europe 1993, OnePetro. https://doi.org/10.2118/26693-ms.

Stewart, S., 2006. Implications of passive salt diapir kinematics for reservoir segmentation by radial and concentric faults. Mar. Petrol. Geol. 23 (8), 843–853. https://doi.org/10.1016/j.marpetgeo.2006.04.001.

Stewart, S.A., 2007. Salt tectonics in the North Sea Basin: a structural style template for seismic interpreters. Geological Society, London, Special Publications 272 (1), 361–396. https://doi:10.1144/GSL.SP.2007.272.01.19.

Stewart, S.A., Coward, M.P., 1995. Synthesis of salt tectonics in the southern North Sea, UK. Mar. Petrol. Geol. 12 (5), 457–475. https://doi.org/10.1016/0264-8172(95)91502-g.

Tao, Z., Alves, T.M., 2019. Impacts of data sampling on the interpretation of normal fault propagation and segment linkage. Tectonophysics 762, 79–96. https://doi.org/10.1016/j.tecto.2019.03.013.

Taylor, J., 1998. Upper Permian—Zechstein: Petroleum Geology of the North Sea: Basic Concepts and Recent Advances, pp. 174–211. https://doi.org/10.1002/9781444313413.ch6.

Ten Veen, J., Van Gessel, S., Den Dulk, M., 2012. Thin-and thick-skinned salt tectonics in The Netherlands; a quantitative approach. Neth. J. Geosci. 91 (4), 447–464. https://doi.org/10.1017/s0016774600000330.

Teófilo, F.A.F., Junior, E.P., Roehl, D., Martha, L.F., 2018. A numerical approach for investigation of stress states induced by salt structures. Int. J. Rock Mech. Min. Sci. 106, 223–233. https://doi.org/10.1016/j.ijrmms.2018.02.009. van-der-Zee, W.

Van-der-Zee, W., Ozan, C., Brudy, M., and Holland, M., 2011. 3D geomechanical modeling of complex salt structures, in: Proceedings SIMULIA customer conference, p. 1-16.

Van Gent, H., Urai, J.L., De Keijzer, M., 2011. The internal geometry of salt structures–a first look using 3D seismic data from the Zechstein of The Netherlands. J. Struct. Geol. 33 (3), 292–311. https://doi.org/10.1016/j.jsg.2010.07.005.

Van Ojik, K., Silvius, A., Kremer, Y., Shipton, Z., 2020. Fault seal behaviour in Permian Rotliegend reservoir sequences: case studies from the Dutch Southern North Sea. Geological Society, London, Special Publications 496 (1), 9–38. https://doi.org/10.1144/sp496-2018-189.

Van Wees, J.-D., Stephenson, R., Ziegler, P., Bayer, U., McCann, T., Dadlez, R., Gaupp, R., Narkiewicz, M., Bitzer, F., Scheck, M., 2000. On the origin of the southern Permian Basin. Cent. Eur.: Mar. Petrol. Geol. 17 (1), 43–59. https://doi.org/10.1016/s0264-8172(99)00052-5.

Vendeville, B.C., Jackson, M.P.A., 1992. The rise of diapirs during thin-skinned extension. Mar. Petrol. Geol. 9 (4), 331–353. https://doi.org/10.1016/0264-8172(92)90047-i.

Walsh, J.J., Watterson, J., 1988. Analysis of the relationship between displacements and dimensions of faults. J. Struct. Geol. 10 (3), 239–247. https://doi.org/10.1016/0191-8141(88)90057-0.

Warren, J.K., 2017. Salt usually seals, but sometimes leaks: implications for mine and cavern stabilities in the short and long term. Earth Sci. Rev. 165, 302–341. https://doi.org/10.1016/j.earscirev.2016.11.008.

Watterson, J., 1986. Fault dimensions, displacements and growth. Pure Appl. Geophys. 124 (1–2), 365–373. https://doi.org/10.1007/BF00875732.

Wenau, S., Alves, T.M., 2020. Salt-induced crestal faults control the formation of Quaternary tunnel valleys in the southern North Sea. Boreas 49 (4), 799–812. https://doi.org/10.1111/bor.12461.

Wong, T.E., Batjes, D.A., Batjes, D.A.J., 2007. In: de Jager, J. (Ed.), Geology of the Netherlands. Edita Publishing House of the Royal.

Yin, H., Groshong, R.H., 2007. A three-dimensional kinematic model for the deformation above an active diapir. AAPG Bull. 91 (3), 343–363. https://doi.org/10.1306/10240606034.

Zhang, Q., Alves, T.M., Martins-Ferreira, M.A.C., 2022. Fault analysis of a salt minibasin offshore Espírito Santo, SE Brazil: implications for fluid flow, carbon and energy storage in regions dominated by salt tectonics. Mar. Petrol. Geol. 143, 105805 https://doi.org/10.1016/j.marpetgeo.2022.105805.

Ziegler, P., 1990. Collision related intra-plate compression deformations in Western and Central Europe. J. Geodyn. 11 (4), 357–388. https://doi.org/10.1016/0264-3707(90)90017-o.